Kinetics, subcellular localization, and contribution to parasite virulence of a *Trypanosoma cruzi* hybrid type A heme peroxidase (*Tc*APx-CcP)

Martín Hugo[a,b,1,2], Alejandra Martínez[a,b,1], Madia Trujillo[a,b], Damián Estrada[a,b], Mauricio Mastrogiovanni[a,b], Edlaine Linares[c], Ohara Augusto[c], Federico Issoglio[d], Ari Zeida[d], Darío A. Estrín[d], Harry F. G. Heijnen[e], Lucía Piacenza[a,b,3], and Rafael Radi[a,b,3]

[a]Departamento de Bioquímica, Facultad de Medicina, Universidad de la República, Montevideo 11800, Uruguay; [b]Center for Free Radical and Biomedical Research, Universidad de la República, Montevideo 11800, Uruguay; [c]Departamento de Bioquímica, Instituto de Química, Universidade de São Paulo, 05508-000, Sao Paulo, Brazil; [d]Departamento de Química Inorgánica, Analítica y Química-Física and Instituto de Química Física de Materiales, Medio Ambiente y Energía (INQUIMAE), Consejo Nacional de Investigaciones Científicas y Técnicas (CONICET), Facultad de Ciencias Exactas y Naturales, Universidad de Buenos Aires, C1428EHA Buenos Aires, Argentina; and [e]Department of Clinical Chemistry and Hematology, Cell Microscopy Core, University Medical Center, 3584CX Utrecht, The Netherlands

Contributed by Rafael Radi, November 10, 2016 (sent for review September 30, 2016; reviewed by Anibal Vercesi and Shane R. Wilkinson)

The *Trypanosoma cruzi* ascorbate peroxidase is, by sequence analysis, a hybrid type A member of class I heme peroxidases [*Tc*APx-cytochrome *c* peroxidase (CcP)], suggesting both ascorbate (Asc) and cytochrome *c* (Cc) peroxidase activity. Here, we show that the enzyme reacts fast with H_2O_2 ($k = 2.9 \times 10^7$ $M^{-1}{\cdot}s^{-1}$) and catalytically decomposes H_2O_2 using Cc as the reducing substrate with higher efficiency than Asc ($k_{cat}/K_m = 2.1 \times 10^5$ versus 3.5×10^4 $M^{-1}{\cdot}s^{-1}$, respectively). Visible-absorption spectra of purified recombinant *Tc*APx-CcP after H_2O_2 reaction denote the formation of a compound I-like product, characteristic of the generation of a tryptophanyl radical-cation ($Trp^{233\bullet+}$). Mutation of Trp^{233} to phenylalanine (W233F) completely abolishes the Cc-dependent peroxidase activity. In addition to $Trp^{233\bullet+}$, a Cys^{222}-derived radical was identified by electron paramagnetic resonance spin trapping, immunospin trapping, and MS analysis after equimolar H_2O_2 addition, supporting an alternative electron transfer (ET) pathway from the heme. Molecular dynamics studies revealed that ET between Trp^{233} and Cys^{222} is possible and likely to participate in the catalytic cycle. Recognizing the ability of *Tc*APx-CcP to use alternative reducing substrates, we searched for its subcellular localization in the infective parasite stages (intracellular amastigotes and extracellular trypomastigotes). *Tc*APx-CcP was found closely associated with mitochondrial membranes and, most interestingly, with the outer leaflet of the plasma membrane, suggesting a role at the host–parasite interface. *Tc*APx-CcP overexpressers were significantly more infective to macrophages and cardiomyocytes, as well as in the mouse model of Chagas disease, supporting the involvement of *Tc*APx-CcP in pathogen virulence as part of the parasite antioxidant armamentarium.

Trypanosoma cruzi | heme peroxidase | oxidants | virulence | kinetics

The protozoan parasite *Trypanosoma cruzi* is the causative agent of Chagas disease (CD; also known as American trypanosomiasis). Up to 10 million people across Latin America are infected with this protozoan parasite, a distribution range that is expanding driven by migration of infected insects and hosts, with CD now emerging as a public health problem at nonendemic sites (1, 2). *T. cruzi* strains are heterogeneous, exhibiting a high degree of biochemical and genetic variability. Such differences are believed, at least in part, to be responsible for disease outcome, which ranges from being asymptomatic during the course of infection to fatal severe cardiac and digestive complications (3). It has been shown that the parasite antioxidant systems are essential for parasite survival and establishment of the infection in the vertebrate host (4–7). In contrast to most eukaryotes, *T. cruzi* lacks catalase and selenium-dependent glutathione peroxidases, which are enzymes capable of rapidly metabolizing high levels of H_2O_2 (8, 9). Instead, it expresses an array of complex enzyme-mediated mechanisms in which the trypanosomatid-specific thiol trypanothione ([$T(SH)_2$], N^1,N^8-bisglutathionylspermidine) plays a central role in the funneling of reducing equivalents to the different peroxidase antioxidant systems (10). Two typical 2-Cys peroxiredoxins are located in the cytosol (CPX) and in the mitochondrial matrix (MPX), respectively, and efficiently scavenge H_2O_2, peroxynitrite, and small-chain organic hydroperoxides (11–13). Two glutathione-dependent peroxidases are located at the endoplasmic reticulum (ER) and in the cytosol, and seem to be important in the metabolization of lipid-derived hydroperoxides (14). Finally, a plant-like related heme peroxidase located at the ER displays ascorbate (Asc)-dependent peroxidase activity (APx) (15).

Because the *T. cruzi* antioxidant defense systems are distinct from its mammalian host, the trypanosomal activities are suitable targets for specific rationale pharmacological inhibition. During its life cycle, *T. cruzi* undergoes various morphological and biochemical changes. One of the most complex transformations occurs during

Significance

Trypanosoma cruzi, the causative agent of Chagas disease, affects 8–10 million people in Latin America. Parasite antioxidant systems are essential for parasite survival and infectivity in the vertebrate host. Herein, we characterized the enzymic properties, subcellular localization, and contribution to parasite virulence of a *T. cruzi* hybrid type A member of class I heme peroxidases. The enzyme reacts fast with hydrogen peroxide and utilizes both ferrocytochrome *c* and ascorbate as reducing substrates [*T. cruzi* ascorbate peroxidase (*Tc*APx)-cytochrome *c* peroxidase (CcP)]. A unique subcellular distribution of *Tc*APx-CcP in the infective stages suggests a role during parasite–host interactions. Infection of macrophages and cardiomyocytes, as well as in mice, confirmed the involvement of *Tc*APx-CcP in pathogen virulence as part of the parasite antioxidant armamentarium.

Author contributions: M.H., A.M., M.T., L.P., and R.R. designed research; M.H., A.M., D.E., M.M., E.L., O.A., F.I., A.Z., D.A.E., H.F.G.H., and L.P. performed research; M.H., A.M., M.T., D.E., M.M., O.A., F.I., A.Z., D.A.E., H.F.G.H., L.P., and R.R. analyzed data; and L.P. and R.R. wrote the paper.

Reviewers: A.V., Universidade de Campinas; and S.R.W., Queen Mary University of London.

The authors declare no conflict of interest.

[1]M.H. and A.M. contributed equally to this work.

[2]Present address: Department of Molecular Toxicology, German Institute of Human Nutrition Potsdam-Rehbruecke (DIfE), 14558 Nuthetal, Germany.

[3]To whom correspondence may be addressed. Email: rradi@fmed.edu.uy or lpiacenza@fmed.edu.uy.

This article contains supporting information online at www.pnas.org/lookup/suppl/doi:10.1073/pnas.1618611114/-/DCSupplemental.

metacyclogenesis, the process where a noninfective and replicative insect-derived epimastigote cell transforms to a highly infectious, nonreplicative, metacyclic trypomastigote. During this process, it has been shown that *T. cruzi* up-regulates several antioxidant enzymes to preadapt to the hostile environment of the vertebrate host (5, 16, 17). Enzymes known to be up-regulated during this differentiation process include peroxiredoxins, [$T(SH)_2$] synthase (5), Fe-containing superoxide dismutases, and APx (16).

T. cruzi ascorbate peroxidase (*Tc*APx) was first reported to reduce H_2O_2 catalytically in the presence of Asc as the reducing substrate (APx activity), but with a catalytic efficiency several fold lower than plant APx (18, 19). Its overexpression confers parasite resistance toward exogenously added H_2O_2 toxicity (13, 15, 20). Recent studies have shown that *T. cruzi* lacking *Tc*APx is still capable of infecting cultured mammalian cells, albeit at a reduced level, and can still establish an infection in the mouse model of CD (20). Although the enzyme does not seem to be essential for parasite infectivity, its enhanced expression may represent an additional skill for the parasite to deal with host-derived oxidant toxicity both in the acute and chronic stages of the disease (6, 21).

*Tc*APx shares significant homology (62% identity and 86% similarity) with its *Leishmania major* peroxidase (*Lm*P) counterpart (18). Both parasite enzymes are related to the class I heme-peroxidase group of antioxidant enzymes that includes catalase-peroxidase (katG), APx, cytochrome *c* peroxidase (CcP), and the hybrid type (A and B) peroxidases (22). Phylogenetic studies have classified the *T. cruzi* and *Leishmania* enzymes as members of the hybrid type A, subfamily A1, heme peroxidases (23), with other sequences in this group displaying both Asc- and cytochrome *c* (Cc)-dependent peroxidase activities (22, 24). Based on this fact, we have renamed *Tc*APx as *Tc*APx-CcP. These hybrid type A peroxidases represent a real turning point in the evolution of ancient bifunctional catalase-peroxidase toward monofunctional specialization within this family, and their biochemical characterization may help to unravel the evolution of structure–function relationships of these abundant oxidoreductases (23).

*Lm*P can use both Asc (as monofunctional APx) and Cc (as monofunctional CcP) as electron donors (25). H_2O_2 reacts with the heme generating the oxoferryl ($Fe^{IV=O}$) and the porphyrin-centered radical ($P^{\bullet+}$) forming the classical compound I species. The presence of tryptophan located near the heme (Trp^{208} in *Lm*P) rapidly reduces the $P^{\bullet+}$, generating an amino acid-derived cation radical ($Trp^{208\bullet+}$, compound I-like). Finally, using either Asc or Cc as the reducing substrate, the enzyme recovers the resting state (Fe-III-P). Classical compound I formation in these hybrid type A peroxidases was established by direct electron paramagnetic resonance (EPR) analysis (25) and/or by spectroscopic studies using a W208F mutant (25, 26). To date, *Lm*P represents the only trypanosomatid hybrid type A peroxidase characterized as using Asc and Cc as electron donors, with its activity implicated in parasite differentiation and oxidative stress protection (27). Biochemical characterization of other members of this family of peroxidases may help to unravel the catalytic mechanism of these ancient enzymes as well as to define their role in pathogen survival, proliferation, and virulence.

In the present work, we characterized the Cc-dependent peroxidase activity of *Tc*APx-CcP. After a fast reaction with H_2O_2, an intramolecular electron transfer (ET) pathway at the heme microenvironment necessary for the oxidation of Cc was revealed; indeed, in addition to Trp, the role of a Cys residue typically located in the active site of these hybrid type A peroxidases was disentangled. Also, in light of its CcP activity and the presence of a secretory motif, which predicts membrane localization in all other hybrid type A members studied (15, 22, 23), we explored the subcellular localization of the enzyme in the infective *T. cruzi* parasite stages. Finally, the role of *Tc*APx-CcP overexpression in parasite virulence was assessed through in vitro and in vivo infections in the cellular and acute murine model of CD.

Results

Visible Spectral Studies of *Tc*APx-CcP Reaction with H_2O_2. Recombinant *T. cruzi* wild-type (wt) and W233F APx-CcP were purified to homogeneity (>99% pure) by affinity chromatography as assayed by SDS/PAGE (Fig. 1*A* and Fig. S1*A*). For all purifications *ca.* 70% of protein had Fe incorporated (as determined by the Soret peak absorbance in relation to the total protein content). To investigate the reaction of *Tc*APx-CcP with H_2O_2, the optical spectra of *Tc*APx-CcP (from 350 to 650 nm) were recorded before and after the addition of equimolar concentrations of H_2O_2 to assay the spectral shifts associated with the formation of a compound I-like product (Fig. 1*B*). The resting enzyme exhibited a Soret peak at 409 nm that shifted to 420 nm after reaction with H_2O_2, with the appearance of two humps at 539 and 560 nm. These changes in the optical spectra are indicative of the generation of a compound I-like product (25, 26, 28) (Fig. 1*B*). When the W233F mutant was analyzed, the Soret peak was found to be at 414 nm in the resting state, indicating some structural perturbation at the heme microenvironment due to the amino acid replacement (Fig. 1*C*). Upon reaction with H_2O_2, the Soret peak shifted to 418 nm, with only the 560-nm hump now present (Fig. 1*C*). Given the rapid generation of the compound I-like product, rapid kinetics analysis by stopped flow at 10 °C was performed to visualize the classical compound I in *Tc*APx-CcP. The maximal absorption (Soret peak) in the ferric state of heme peroxidases drops in intensity when the enzyme reacts with H_2O_2 to form compound I, so a decrease in absorbance at the Soret peak is expected after H_2O_2 reaction (26, 28, 29). A very fast decay in absorbance for the wt enzyme (Soret peak at 409 nm) was observed upon mixing with H_2O_2, indicating the formation of the $Fe^{IV=O}$-$P^{\bullet+}$ radical of compound I (Fig. 1*D*). Interestingly, data in Fig. 1*E*, show that in the *T. cruzi* W233F mutant, a very fast (5 ms) and minor decay in absorbance at the Soret peak (414 nm) was followed by a slower increase in absorbance, suggesting the generation of an "alternative compound I-like" species. The drop in absorbance at 414 nm for the W233F mutant is in agreement with the spectral data shift upon H_2O_2 addition shown in Fig. 1*C*. Because the compound I was not stabilized

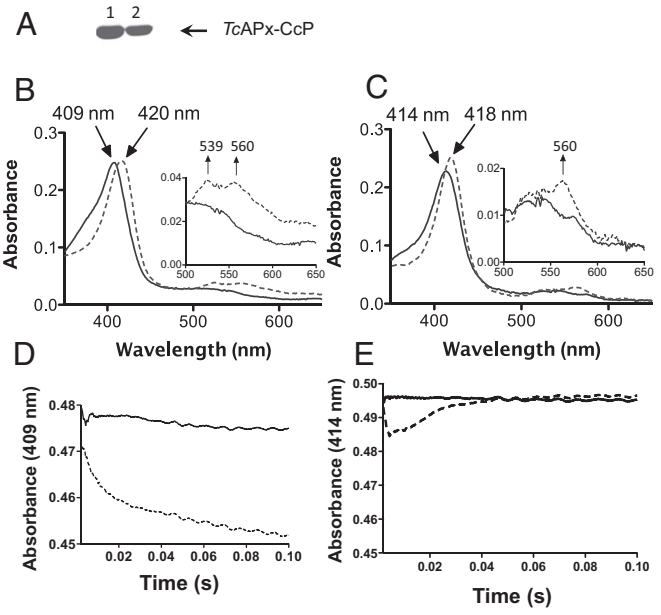

Fig. 1. Spectroscopic analysis of *Tc*APx-CcP compound I and compound I-like intermediates. (*A*) SDS/PAGE of purified, recombinant *Tc*APx-CcP (1) and its W233F mutant (2) visualized following Coomassie blue staining. Absorption spectra of *Tc*APx-CcP (2 μM) (*B*) and the W233F mutant (*C*) before (solid line) and after (dashed line) equimolar H_2O_2 addition (2 μM). (*Inset*) Spectra from 500 to 650 nm. Arrows indicate the Soret peak of the resting enzyme and after H_2O_2 reaction. Spectral shifts of *Tc*APx-CcP are indicative of compound I-like formation. *Tc*APx-CcP (5 μM) (*D*) or W233F (*E*) was mixed with (dashed line) or without (solid line) H_2O_2 (5 μM) at 10 °C. Changes in the absorbance at the Soret peak [409 and 414 nm for *Tc*APx-CcP (*D*) and W233F (*E*), respectively] were followed. The decrease in the absorbance at the Soret peak is indicative of compound I generation.

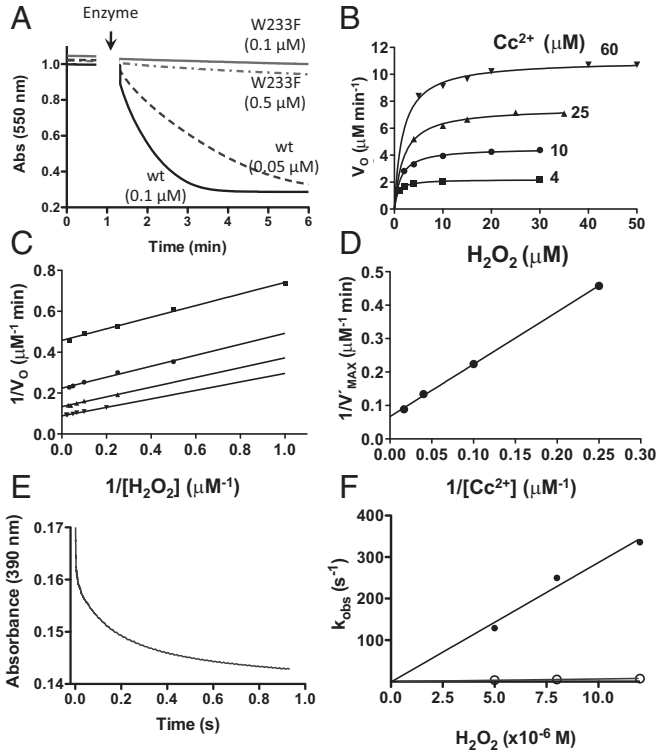

Fig. 2. Investigating the Cc-dependent peroxidase activity of *Tc*APx-CcP. (*A*) Oxidation of Cc^{2+} (50 μM) was followed at 550 nm in the presence of H_2O_2 (10 μM) before and after the addition of *Tc*APx-CcP (wt; solid and dashed black lines, respectively) or its W233F mutant (solid and dashed gray lines, respectively). Proteins concentrations are noted, whereas the arrow indicates when enzyme was added to each reaction. Abs, absorbance. (*B*) Activity assay described in *A* was performed in the presence of *Tc*APx-CcP (0.05 μM) using different concentrations of H_2O_2 (0–50 μM) and Cc^{2+} (4, 10, 25, and 60 μM). The continuous lines show the best fit to a rectangular hyperbola for the experimental data. Double reciprocal (*C*) and secondary (*D*) plots from the data obtained in *B*. (*E*) *Tc*APx-CcP (2 μM) was mixed in the stopped-flow spectrophotometer with H_2O_2 (8 μM) in sodium phosphate buffer (100 mM, pH 7.4) containing DTPA (0.1 mM) at 25 °C. The time-dependent change in absorbance at 390 nm (maximal absorbance difference observed for resting and oxidized enzymes; Fig. 1*B*) was followed. (*F*) Effect of H_2O_2 concentrations on the observed rate constants of the biphasic decay (at 390 nm). Filled (●) and empty (○) circles represent fast and slow phases of decay, respectively. The continuous lines represent the best linear fit of experimental data. Data shown are from a representative experiment reproduced three times.

in the W233F mutant, the data support that other amino acids, in addition to Trp^{233}, can participate in the reduction of the Fe-$^{IV=O}$-$P^{\bullet+}$ radical in *Tc*APx-CcP.

Kinetic Analysis of the Cc-Dependent Peroxidase Activity. Both the formation of a compound I-like product (this work) and the phylogenetic analysis of *Tc*APx-CcP indicate that the *T. cruzi* enzyme might function using Asc and Cc as electron donors. The *Tc*APx-CcP activity with Cc as the reducing substrate was monitored spectrophotometrically at 550 nm following ferrocytochrome *c* (Cc^{2+}) oxidation after H_2O_2 addition. As shown in Fig. 2*A*, Cc^{2+} oxidation was observed in the presence of variable concentrations of wt enzyme (0.05–0.1 μM) after H_2O_2 addition (50 μM). When the W233F enzyme was used, even at high concentrations (0.1–0.5 μM), no Cc^{2+} oxidation was observed, indicating the central role of Trp^{233} for the Cc-dependent enzyme activity (Fig. 2*A*). In this mutant, a 10-fold decrease in Asc-dependent activity was also measured. To characterize the Cc-dependent peroxidase activity further, steady-state kinetic analysis was performed in the presence of wt *Tc*APx-CcP (0.05 μM), and variable amounts of Cc^{2+} (0–60 μM) and H_2O_2 (0–50 μM) as shown in Fig. 2*B*. The activity of the wt enzyme obeys Michaelis–Menten kinetics as assessed by the dependency of the initial velocity (V_0) as a function of H_2O_2 concentration under different Cc^{2+} concentrations (Fig. 2*B*). A secondary plot of $1/V_0$ vs. $1/[H_2O_2]$ generated linear parallel slopes, indicating that *Tc*APx-CcP displays a typical bisubstrate ping-pong kinetic mechanism (30, 31) (Fig. 2*C*). From the *y*-axis intercept, apparent V_{max} (V'_{max}) values for the different Cc^{2+} concentrations used were calculated. From the *y*- and *x*-axis intercepts of the secondary plot ($1/V'_{max}$ vs. $1/[H_2O_2]$; Fig. 2*D*), $1/V_{max}$ and $1/K_m$ values for Cc^{2+} were determined, respectively: K_m (Cc^{2+}) = 23.5 μM, k_{cat} = 5.0 s^{-1}, and k_{cat}/K_m (Cc^{2+}) = 2.1 × 10^5 $M^{-1}{\cdot}s^{-1}$. To determine the rate constant of the enzyme with H_2O_2, the absorbance at 390 nm (a λ value at which the resting and oxidized enzyme have significant absorbance differences; Fig. 1*B*) was followed by rapid stopped-flow techniques. The reaction of H_2O_2 (8 μM) with *Tc*APx-CcP (2 μM) led to a fast time-dependent decrease in absorbance (Fig. 2*E*). The time course was fitted to a double exponential decay, with observed rate constants for both phases dependent on H_2O_2 concentration (Fig. 2*F*). The slopes of the plot (Fig. 2*F*) yielded second-order rate constants for the H_2O_2-dependent oxidation of *Tc*APx-CcP of (2.9 ± 0.5) × 10^7 $M^{-1}{\cdot}s^{-1}$ and (5.4 ± 0.2) × 10^5 $M^{-1}{\cdot}s^{-1}$ for the fast and slow processes, respectively. The *k* value on the order of 10^7 $M^{-1}{\cdot}s^{-1}$ for the initial reaction of H_2O_2 with the resting ferric state of the *Tc*APx-CcP is in good agreement with previous reports for other heme peroxidases (26, 32). It was previously shown that APx enzymes (in the absence of reducing substrates) are inactivated by H_2O_2 (33). Thus, the slower process is likely to represent (because no reducing substrate was present) the reaction of a second molecule of H_2O_2 with the oxidized *Tc*APx-CcP species, leading to an inactive form of the enzyme. Indeed, under these experimental conditions, we also observed a time-dependent inactivation of the enzyme by H_2O_2 (*SI Materials and Methods* and Fig. S1). In Table 1, the parameters of the steady-state kinetic analysis at pH 7.4 of *Tc*APx-CcP when using Cc (Fig. 2) or Asc (Fig. S2) as the reducing substrates are shown. Overall, the efficiency of *Tc*APx-CcP when using Cc is one order of magnitude higher than with Asc.

Detection of *Tc*APx-CcP $Trp^{233\bullet+}$ Radical and Role of Cys^{222}. To determine the amino acid-derived radicals participating in the *Tc*APx-CcP catalytic cycle after reaction with H_2O_2, EPR spin trapping studies were carried out. Upon addition of equimolar concentrations of H_2O_2 to the wt enzyme (60 μM) in the presence of the spin trap 3,5-dibromo-4-nitroso benzene sulfonate (DBNBS) (10 mM), an immobilized carbon-centered radical adduct signal that has a nitrogen hyperfine splitting constant (a_N) value of 32 G (or $2a_N$ = 64 G); this signal was absent in the W233F mutant (Fig. 3). Overall, these results strongly support the participation of a Trp^{233}-derived radical in the generation of the compound I-like product. Detailed inspection of the heme microenvironment in hybrid type A and CcP peroxidases revealed the presence of a Cys residue (Cys^{222} for *T. cruzi* enzyme) located near Trp^{233} (25, 34); this Cys residue is absent in the APx family (23). It has been proposed that the sulfur atom of this Cys residue favors stabilization of the *Lm*P compound I-like product. Indeed, mutation of Cys^{197} to Thr in *Lm*P decreased more than 100-fold the Cc^{2+}-dependent peroxidase activity without affecting the Asc-dependent function (25, 26). We thus explored the involvement of Cys^{222} in *Tc*APx-CcP peroxidase activity by means of alkylation of enzyme thiols with *N*-ethyl-maleimide

Table 1. Steady-state kinetic parameters for *Tc*APx-CcP

Substrate	K_m, μM	k_{cat}/K_m, $M^{-1}{\cdot}s^{-1}$	pH	Source
Asc	192 ± 19	5.7 × 10^4	6.5	(15)
	190 ± 2	3.5 × 10^4	7.4	This work
Cc	29 ± 8	2.1 × 10^5	7.4	This work

(NEM). Of the six Cys residues present in *Tc*APx-CcP, two are buried in the protein structure and four (including Cys^{222}) are solvent-accessible. As shown in Fig. 4, NEM-treated wt enzyme reacts with H_2O_2 (as wt nontreated enzyme) with the generation of a compound I-like product (Fig. 4*A*). Although the NEM-treated enzyme reacted with H_2O_2, Cc^{2+}-dependent peroxidase activity was decreased by more than 70% compared with wt enzyme, although the Asc-dependent peroxidase activity was not affected (25, 26) (Fig. 4*D*). Interestingly, when the NEM-treated W233F mutant was exposed to H_2O_2, no changes in the Soret peak at 414 nm of the resting Fe-III was observed (Fig. 4*C*). In this condition, a significant drop in Asc-dependent peroxidase activity was also evident for the W233F-NEM enzyme (Fig. 4*D*). Overall, the above results indicate that Cys^{222} (located near the heme and Trp^{233}) is necessary for compound I-like generation/stability.

To determine the generation of a Cys^{222} radical accurately after reaction of *Tc*APx-CcP with H_2O_2, immunospin trapping assays using 5,5-dimethyl-1-pyrroline-*N*-oxide (DMPO) were performed. Untreated or NEM-treated wt and W233F enzymes (10 μM) were exposed to H_2O_2 (0–30 μM) in the presence of DMPO (100 mM). DMPO-protein adducts were evaluated by Western blot using the anti–DMPO-nitrone antibody as previously reported (35). In the wt enzyme, DMPO-nitrone adducts were observed with a signal intensity dependent on H_2O_2 concentration (Fig. 5*A*). These immunoreactive signals were completely abrogated in the NEM-treated enzyme, strongly suggesting the participation of Cys in the detected protein adduct (Fig. 5*A*). Moreover, the signal was greatly enhanced in the W233F mutant, suggesting that in the absence of Trp^{233}, Cys^{222} could be involved in the recovery of compound I, leading to an alternative ET pathway, as suggested from data in Fig. 1*D*. These results were corroborated by EPR spin trapping analysis (Fig. 5*B*). Reaction of the wt enzyme (60 μM) with equimolar concentrations of H_2O_2 in the presence of DMPO (100 mM) yielded a detectable paramagnetic signal; notably, the EPR signal was significantly enhanced in the W233F mutant (Fig. 5*B*, line B). One hyperfine splitting constant of the beta hydrogen (a^H_β) of the adduct signal (a^H_β = 16 G) is fully consistent with the trapping of an APx-CcP-cysteinyl radical, whereas another (a^H_β = 9.3 G) suggests that a Tyr radical may be also trapped (36, 37). Furthermore, the formation of the DMPO radical adduct was almost fully inhibited in the NEM-treated wt and W233F enzymes (Fig. 5*B*, lines *C*). The results indicate the generation of a protein-derived radical located at the active site Cys^{222} (alternative compound I-like) that is important for the *Tc*APx-CcP Cc-dependent peroxidase activity (Fig. 4*B*). To obtain full confirmation of the formation of Cys^{222} radical upon H_2O_2 reaction, peptide mapping-MS analysis of *Tc*APx-CcP was performed. A manual search for the peptide of interest revealed both L^{203}-K^{237} and DMPO-adduct peptides coeluting at 60.2 min. Most abundant ions were those ions tetra-charged for both peptides

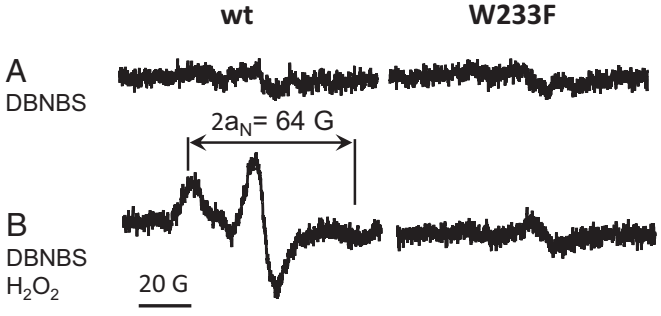

Fig. 3. EPR spectra of DBNBS radical adducts obtained for oxidized *Tc*APx-CcP. The spectra were obtained after reaction of *Tc*APx-CcP (wt) and the W233F enzyme (60 μM) in DBNBS (10 mM) in the absence (*A*) or presence (*B*) of H_2O_2 (60 μM). $2a_N$, the distance between the external peaks in G corresponds to twice the value of the hyperfine splitting constant of the nitrogen atom of the radical adduct ($2a_N$ = 64 G).

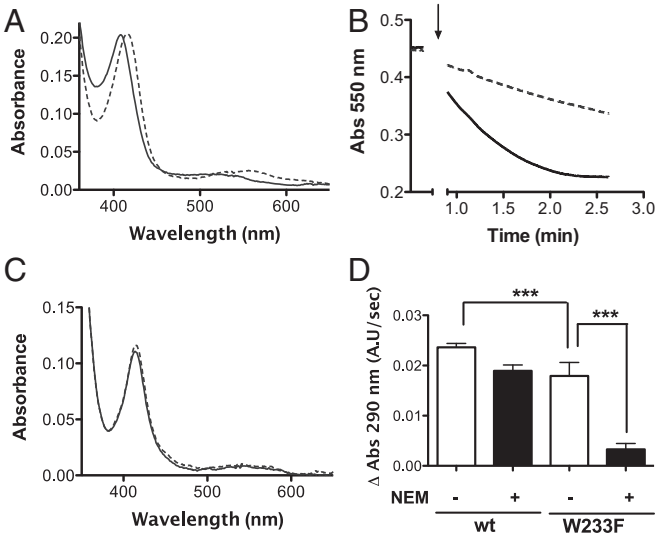

Fig. 4. Peroxidase activity of *Tc*APx-CcP following cysteine alkylation. (*A*) Spectral change of resting, NEM-treated (solid line; Soret peak at 409 nm), or H_2O_2-treated (2 μM; dashed line; Soret peak at 420 nm) *Tc*APx-CcP (2 μM). (*B*) Cc^{2+}-dependent peroxidase activity of untreated (solid line) and NEM-treated (dashed line) *Tc*APx-CcP (0.01 μM) toward H_2O_2 (20 μM) using Cc^{2+} (20 μM) as a reductant. Activity was followed by monitoring the change in absorbance at 550 nm. The arrow indicates the addition of enzyme. (*C*) Spectral change of resting, NEM-treated (solid line), or H_2O_2-treated (2 μM; dashed line) *Tc*APx-CcP W233F (2 μM; Soret peak at 414 nm). (*D*) Asc-dependent peroxidase activity of *Tc*APx-CcP (0.13 μμM) and the W233F mutant (1 μM), with (+) or without (–) NEM treatment, toward H_2O_2 (40 μM). Assays were conducted in the presence of Asc (200 μM), and activity was monitored by following the change in absorbance at 290 nm. Data represent the mean ± SEM from five independent determinations and are expressed as absorbance units per second. ***P < 0.0001 by one-way ANOVA and post-Tukey's multiple comparison test.

although triple-charged ions were also found. Enhanced resolution analysis was performed for best accuracy and mass-to-charge ratio (m/z) were obtained for each peptide: 1,258.9 ($[M + 3H]^{3+}$); 944.4 ($[M + 4H]^{4+}$); 1,294.9 ($[M + DMPO + 3H]^{3+}$); 971.4 ($[M + DMPO + 4H]^{4+}$). The fragmentation pattern of the DMPO-peptide adduct was obtained by an enhanced product ion of m/z 971.4 (Fig. 5*C*). Several b and y ions were found, ensuring identity of the peptide sequence. Interestingly, the y-series (y_9–y_{15} ions) suggests that Tyr^{229} is unmodified after treatment with H_2O_2 in the presence of DMPO. The assignment of the DMPO-modified amino acid was finally obtained with the data of the b_{17} fragment (unmodified peptide) and the b_{22} fragment (modified peptide) in full support of Cys^{222} as the preferential site of adduct formation by DMPO in the W233F enzyme (Fig. 5*C*). Overall, EPR spin trapping, immunospin trapping, and peptide mapping-MS data support the critical role of Cys^{222} in the generation of the alternative compound I-like in *Tc*APx-CcP.

Molecular Dynamics of ET Pathways at the Heme Microenvironment Involving Trp^{233} and Cys^{222}. Using the previously reported crystallographic structure of *Lm*P [Protein Data Bank (PDB) ID code 3RIV], we performed homology models for the *Tc*APx-CcP (25) (Fig. S3), from which 100-ns-long molecular dynamics (MD) simulations were conducted. The proximal site of the heme in *Tc*APx-CcP contains the conserved residues Trp^{233}, Cys^{222}, and His^{217} present in all hybrid type A peroxidases (23). The critical Trp^{233} side chain is maintained nearby the His^{217} that coordinates the heme iron via π-stacking interactions (Fig. 6). This structural property determines the capability of Trp^{233} of being able to reduce the heme after its reaction with H_2O_2. Particularly for *Tc*APx-CcP, Trp^{233} is located close to Cys^{222}. MD simulations indicate that the interactions between the Trp^{233} and Cys^{222} side chains are influenced by the thiol or thiolate character of Cys^{222} (i.e., Cys^{222} pK_a). The thiol form shows a

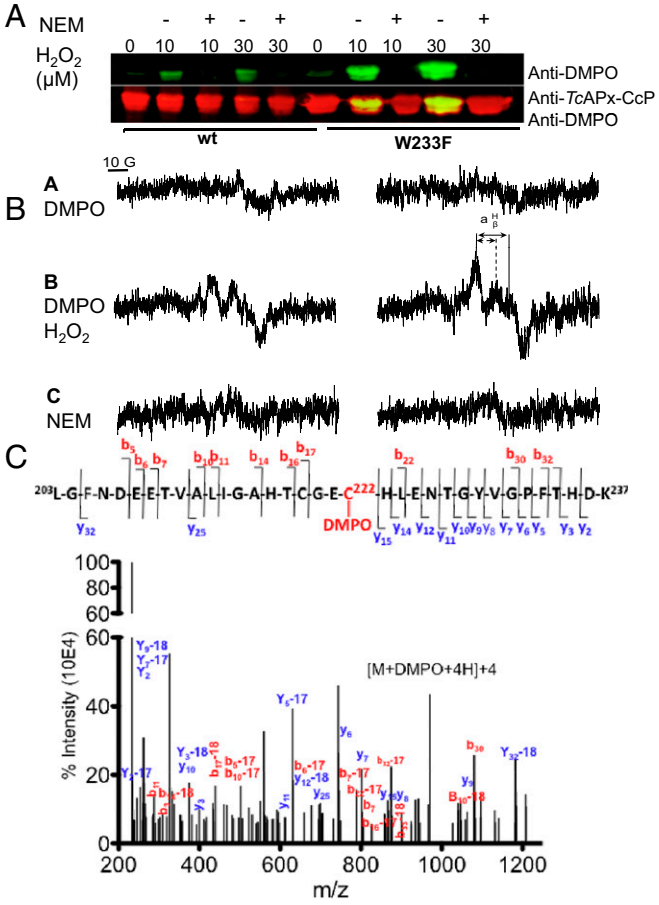

Fig. 5. Immunospin trapping, EPR spectra, and mass spectrometry analysis of *Tc*APx-CcP protein adducts in the presence of DMPO. (*A*) Blot containing *Tc*APx-CcP and W233F mutant (10 μg) protein, with (+) or without (–) NEM treatment, treated with H_2O_2 (0, 10, and 30 μM) in the presence of DMPO (100 mM) was probed with anti-DMPO antibody (green) to detect protein-DMPO-nitrone adducts and anti–*Tc*APx-CcP antisera (red). Merging (*Tc*APx-CcP plus DMPO) is shown in yellow. (*B*) EPR spectra of *Tc*APx-CcP (wt, *Left*) and the W233F mutant (*Right*, 60 μM each) in the presence of DMPO (100 mM) before (line A) and after (line B) the addition of H_2O_2 (60 μM). Line C is the same as line B, except the enzymes were NEM-treated. A composite signal with values of the hyperfine splitting constant of the hydrogen atom (a^H_β) of adducts of 9.4 G and 16 G is consistent with trapping of tyrosyl and cysteinyl radicals, respectively. (*C*) Tandem MS analysis of the *Tc*APx-CcP-DMPO adduct. The spectrum of the tetra-charged ion at *m/z* 971.1 (retention time = 60.2 min) from a tryptic digestion of the *Tc*APx-CcP W233F mutant (16 μM) after treatment with equimolar H_2O_2 in the presence of DMPO (100 mM) is shown. The major N-terminal (b, red-labeled) and C-terminal (y, blue-labeled) fragment ions that allowed the sequence L203-K237 assignment containing a cysteine-linked DMPO residue are shown. The upper part of *C* shows the amino acid sequence of peptide L203-K237, indicating major b and y ions detected by EPI.

direct interaction with Trp^{233}, but also with the heme porphyrin aromatic system mainly in the form of thiolate (Fig. 6 and Fig. S4*A*). To understand the redox interplay at the heme microenvironment involving the heme, Trp^{233}, and Cys^{222} better, we performed ET probability calculations by using the "pathways" formalism. By means of this method, the possible paths for ET from Trp^{233} and Cys^{222} to the oxoferryl heme were computed throughout the MD trajectories. The best possible structural path (i.e., the higher electronic coupling matrix) connecting the electron donor and acceptor was obtained, allowing us to analyze and compare key structural features governing the ET process. In Fig. S4*B*, the average values are shown. The data support that the preferred ET pathway involved the heme-dependent oxidation of Trp^{233} (Fig. 7, route A) to the $Trp^{233\bullet+}$ intermediate; this intermediate may lose a proton with the generation of the neutral indolyl radical ($NTrp^{233\bullet}$) to be reduced by Cys^{222} to yield the corresponding cysteinyl radical and establishing a redox equilibrium between the two amino acid-derived radical species. On the other hand, in the W233F mutant, the oxidized heme will promote the direct one-electron oxidation of the thiolate form of Cys^{222} (Fig. 7, route B), thus maintaining the Asc peroxidase activity of the enzyme in the absence of Trp^{233} (Fig. 4*D*).

Subcellular Localization of *Tc*APx-CcP in the Infective Parasite Stages. Here, the kinetic data shown above indicate that the *Tc*APx-CcP–preferred source of reducing equivalents is Cc. In addition to the previously reported ER localization in the noninfective epimastigote stage (15), we searched for the presence of *Tc*APx-CcP in the mitochondrial compartment (where Cc is present) in the different parasite stages (noninfective epimastigotes, infective intracellular amastigotes, and extracellular trypomastigotes) using specific antibodies (Fig. S5). First, and using *Tc*APx-CcP overexpressers (epimastigote), we conducted controlled-digitonin permeabilization studies to evaluate the coelution of the enzyme with mitochondrial markers (Fig. S6*A*). *Tc*APx-CcP was found to coelute with Cc and Fe-superoxide dismutase A (SODA) (mitochondrial markers), and it was also present in the membrane fraction (Fig. S6*A*). This result indicates that at least a fraction of the enzyme is associated with mitochondria. Immunofluorescence microscopy of *T. cruzi* epimastigotes evidences a nonhomogeneous distribution of the enzyme, compatible with ER localization (15). The enzyme is also present in close proximity to mitochondrial DNA and Fe-SODA (Fig. S6*B*). Finally, to localize proteins at the ultrastructural level precisely, providing simultaneous visualization of antigen epitopes together with the ultrastructure of membrane compartments, we conducted immunoelectron microscopy (immuno-EM) (38) of *Tc*APx-CcP in the infective *T. cruzi* stages. *Tc*APx-CcP enzyme was found to be located in mitochondria, particularly associated with membranes of the cristae (Fig. 8*B* and Figs. S7 and S8). The localization of *Tc*APx-CcP in mitochondria was different from the localization observed for MPX located at the mitochondrial matrix (11) (Fig. 8 *C*–*E*). Intriguingly, the enzyme was found to be associated with the plasma membrane of the intracellular amastigote and extracellular trypomastigote stages, potentially forming a "shield" at the host–parasite interface (Fig. 8*A* and Figs. S7 and S8). These observations were confirmed in *T. cruzi* pTEX-APx-9E10

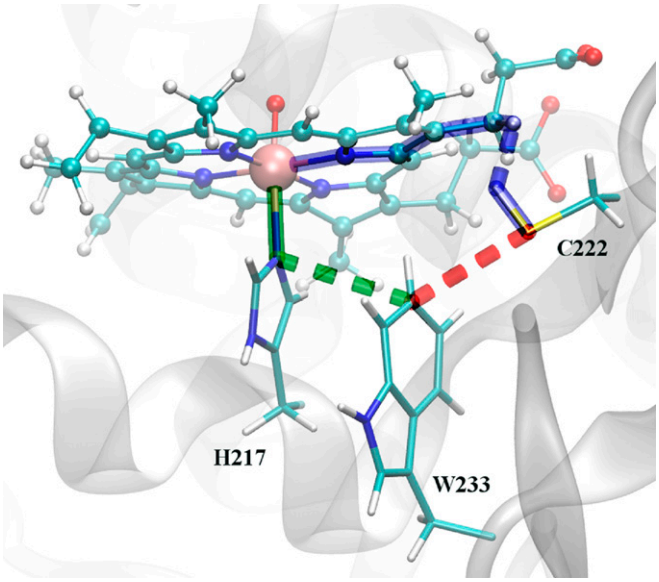

Fig. 6. Predicted ET pathway across the active site of *Tc*APx-CcP. The Trp^{233}→heme, Cys^{222}→heme, and Cys^{222}→Trp^{233} paths are shown in green, blue, and red, respectively.

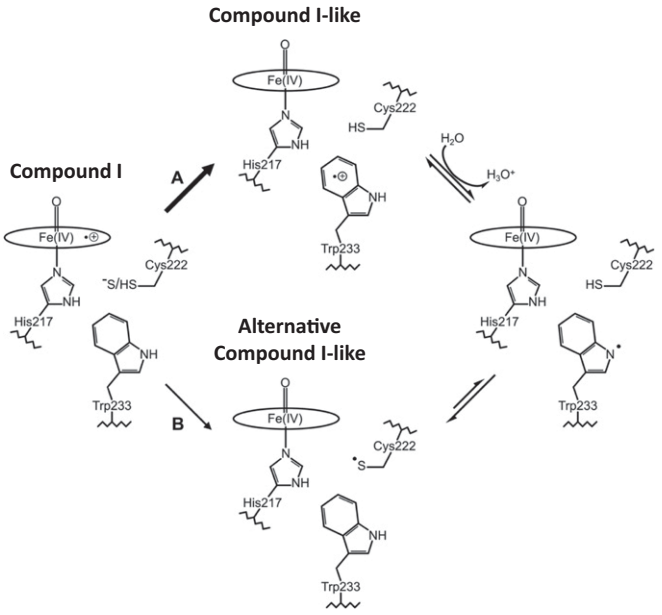

Fig. 7. Representation of the heme microenvironment redox pathways after H_2O_2 reaction with *Tc*APx-CcP. Pathway A shows heme reduction via Trp^{233} with the formation of the tryptophanyl radical (thermodynamically favored pathway), whereas pathway B involves alternative heme reduction via Cys^{222} (in its thiolate form), yielding the corresponding cysteinyl radical. ET between Trp^{233} and Cys^{222} in both pathways is shown. Arrows widths and lengths are indicative of relative flow rates.

overexpressers using the monoclonal anti–c-Myc antibody in both the trypomastigote and amastigote stages (Fig. S7). The presence of *Tc*APx-CcP at the host–parasite interface strongly suggests its participation in the parasite defense mechanisms toward host-derived toxicity. To date, the physiological reducing substrate (i.e., Asc, Cc, or both) for this ancient enzyme in *T. cruzi* is still elusive (*Discussion*).

Enhanced Virulence of *Tc*APx-CcP Overexpressers in Cellular and Mice Infections. *T. cruzi* interaction with macrophages leads to the assembly of the membrane-bound NADPH oxidase with the generation of sustained (90 min) and large amounts of superoxide radical, and thus hydrogen peroxide, directed toward the internalized parasite (7). Once internalized, *T. cruzi* has to deal with the oxidative environment of the phagosome to survive and escape to the host cytosol, where it proliferates as amastigotes. Thus, we first searched for parasite survival in naive macrophage infections. Macrophages were infected with wt or *Tc*APx-CcP–overexpressing trypomastigotes, and infection yields were evaluated after 24 h by intracellular amastigote counting. Trypomastigotes overexpressing *Tc*APx-CcP were more resistant to macrophage toxicity compared with wt parasites, indicating the participation of *Tc*APx-CcP in the H_2O_2 detoxification generated during parasite internalization (Fig. 9*A*). Finally, the infectivity of *Tc*APx-CcP overexpressers was evaluated in cardiomyocytes, cells where amastigotes can reside during chronic infection. It has been shown that *T. cruzi* cardiomyocyte infection leads to the establishment of host–mitochondrial dysfunction, with an increase in H_2O_2 and inflammatory cytokine (IL-1β and TNF-α) production (39). We evaluated the infectivity of *Tc*APx-CcP overexpressers following 96 h of infection, an incubation time sufficient to cause mitochondrial dysfunction in cardiomyocytes and to achieve amastigote replication in the host cell cytoplasm. Rat-derived ventricular cardiomyocytes (H9c2) were infected as above and incubated for 96 h. As was observed for macrophages, *Tc*APx-CcP overexpressers were more infective than wt parasites, supporting the participation of the enzyme in enhancing virulence (Fig. 9*A*). These results correlate well with in vitro studies where *Tc*APx-CcP–null parasites infect myoblast cells at a reduced level (20). Finally, and to validate the enhanced virulence of the *Tc*APx-CcP overexpressers in vivo, we conducted mouse (BALB/c susceptible and C57BL/6 resistance lineages; Fig. 9*B*) infections with culture-derived trypomastigotes from wt (CL-Brener) and *Tc*APx-CcP overexpressers. As shown in Fig. 9*B*, *Tc*APx-CcP overexpressers produced higher blood parasitemias in the acute infection model of CD, indicating the role of this enzyme in parasite virulence and consistent with its function as part of the pathogen defense against host-derived cytotoxic oxidants.

Discussion

By phylogenetic (23) and biochemical studies (this work), *Tc*APx-CcP is a hybrid type A peroxidase sharing both Asc- and Cc-dependent peroxidase activity. Although initially described to use Asc as a reducing substrate (15), the catalytic efficiency with Cc is higher, suggesting that, in vivo, the enzyme may also function as a CcP, so long as a component of *Tc*APx-CcP is present where this "alternative" reducing equivalent is found, such as the mitochondrion. Spectral analysis during the reaction of the enzyme with H_2O_2 showed the formation of a compound-I like (Fig. 1*B*) characteristic of the generation of the $Trp^{233\bullet+}$ in

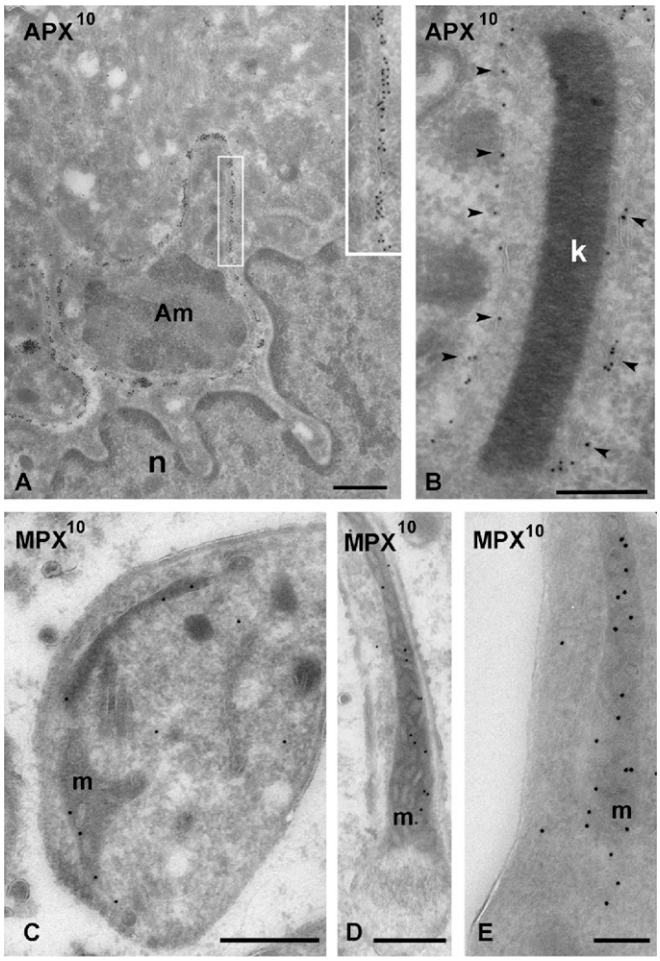

Fig. 8. *Tc*APx-CcP is localized to the plasma membrane and mitochondrion of intracellular *T. cruzi* amastigotes. Cultured cardiomyocytes infected with *T. cruzi* (wt) were analyzed with antisera raised against *Tc*APx-CcP (*A* and *B*) or *Tc*MPX (*C–E*) (APX^{10} and MPX^{10} nm of gold, respectively). The white outlined rectangle shows a high magnification of the amastigote plasma membrane, and black arrowheads indicate amastigote mitochondrial membranes. Am, amistigote; k, kinetoplast; m, mitochondrion; n, nucleus of infected cell. (Scale bars: *A–D*, 500 nm; *E*, 200 nm.)

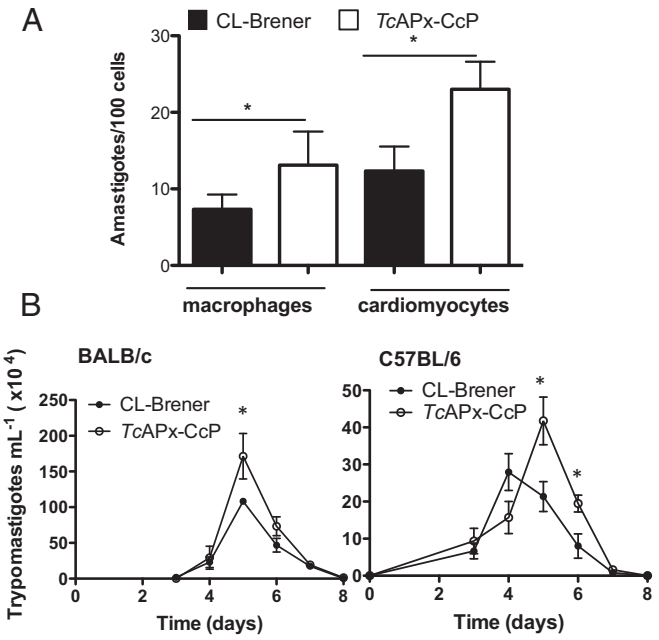

Fig. 9. *Tc*APx-CcP overexpression enhances parasite virulence. (*A*) Culture-derived *T. cruzi* trypomastigotes (CL-Brener and *Tc*APx-CcP overexpressers) were used to infect macrophages at a ratio of five trypanosomes per cell. Following 24 h of infection, cells were stained with DAPI and the number of intracellular amastigotes was counted. Cardiomyocyte infection was performed as above, except that the time of infection was increased to 96 h. Results are expressed as the number of intracellular amastigotes per 100 cells. Data represent the mean ± SEM of at least three independent experiments. (*B*) BALB/c or C57BL/6 mice (five per group) were infected with 1.5×10^7 culture-derived *T. cruzi* trypomastigotes (CL-Brener and *Tc*APx-CcP overexpressers). Blood taken from each mouse at daily intervals from day 3 postinfection onward was microscopically examined for the presence of the bloodstream form of trypomastigotes. Data represent the mean ± SEM for each day. $^*P < 0.005$ as assayed by the Student's *t* test.

these enzymes (25). The classical compound I was transiently detected following fast absorption spectra of the resting enzyme at the Soret peak (409 nm) after the H_2O_2 reaction (Fig. 1*D*). The participation in the reaction of the critical Trp^{233} located in close proximity to the heme was supported by EPR-spin trapping experiments (Fig. 3) and by the site-directed enzyme mutant (W233F) in experiments that included the lack of detection of the EPR signal in parallel with a great drop in the Cc-dependent activity and a 10-fold decrease in Asc-dependent peroxidase activity (Figs. 2 and 4). Rapid UV-visible scanning of the W233F enzyme (Soret peak at 414 nm) permitted detection of an alternative compound I-like species (Fig. 1 *C* and *E*), indicating that another redox-active amino acid located in the heme microenvironment was able to participate rapidly in the one-electron reduction of the porphyrin cation radical present in classical compound I. Protist hybrid type A heme peroxidases contain a Cys residue located near the heme (Cys^{222} and Cys^{197} for *T. cruzi* and *Lm*P, respectively) (22). Immunospin trapping, EPR-spin trapping, and peptide mapping-mass spectrometry analysis using DMPO revealed the presence of a cysteinyl radical in wt *Tc*APx-CcP upon H_2O_2 reaction that was enhanced in the W233F mutant (Fig. 5). Enzyme thiol alkylation dramatically lowered the Cc-dependent peroxidase activity of *Tc*APx-CcP in line with the participation of this residue in enzyme activity. In this sense, MD simulations revealed that in fact, once the $Trp^{233\bullet+}$ is formed to yield the alternative compound I, a subsequent ET can occur with the participation of Cys^{222}. For this ET to occur, once the $Trp^{233\bullet+}$ is formed, it must lose a proton to yield the neutral indolyl radical ($NTrp^{233\bullet}$) that, in turn, can abstract a hydrogen atom for the neutral HS-Cys^{222}, generating a cysteinyl radical (Cys^{222}-$S^\bullet$) (Eq. **1** and Fig. 7), establishing the following equilibrium:

$$NTrp^{233\bullet} + Cys^{222}\text{-}SH \rightleftharpoons HNTrp^{233} + Cys^{222}\text{-}S^\bullet. \qquad [1]$$

It is important to note that the estimated one-electron redox potentials of the iron/oxo complex and the tryptophanyl and cysteinyl radicals are approximately: 1,156, 1,025 and 970 mV, respectively, at pH 7.4 (40, 41), all of which are thermodynamically consistent with preferential route "A" of the ET shown in Fig. 7. In light of these data, we propose that the equilibrium involving the presence of Cys^{222} (Eq. **1**) allows the stabilization of the protein-derived radicals, permitting a more selective reactivity of $Trp^{233\bullet+}$ toward Cc^{2+} after binding of the reducing substrate to the active site. Overall, these observations indicate distinctive characteristics of the *Lm*P enzyme compared with the *T. cruzi* enzyme (e.g., formation of compound-like I in *Tc*-APx-CcP) and provide a detailed atomistic picture of the redox processes occurring at the heme microenvironment during catalysis in this family of peroxidases. Future studies involving crystallization of *Tc*APx-CcP and comparative analysis with *Lm*P should help to rationalize the subtle differences observed herein in the reaction mechanism.

The hybrid type APx-CcP peroxidases have been proposed to represent an evolutionary link between catalase-peroxidase and Cc-peroxidases, although their physiological roles are still under discussion (23). *Lm*P, located at the parasite mitochondria, is involved in H_2O_2 detoxification during parasite differentiation and infectivity (27, 42). In light of its CcP activity, we searched for *Tc*APx-CcP localization in the different *T. cruzi* parasite stages. In addition to the early report of ER localization in the noninfective epimastigote stage, immuno-EM experiments revealed that the enzyme was also associated with the mitochondria cristae in all parasite stages (Fig. 8 and Fig. S7), suggesting that the mitochondrial-associated fraction of the enzyme may truly work as a CcP. In the intracellular amastigotes and extracellular trypomastigotes, *Tc*APx-CcP was also found to be noticeably located at the plasma membrane of the parasite in close interaction with the host cytosol, creating an "antioxidant shield" at the host–parasite interface (Fig. 8). This membrane localization was not evident in the *T. cruzi* epimastigote stage (Fig. S7). In this subcellular localization, *Tc*APx-CcP may principally use host cell-derived Asc as a reductant to protect the parasite from H_2O_2. Overall, we speculate that the infective stage of the parasite uses the reducing substrates alternatively depending on their availability. Although micromolar Asc is found in both the host cytoplasm (43) and *T. cruzi* trypomastigotes (17), micromolar Cc is also present in the mitochondrial intermembrane space (44), supporting that *Tc*APx-CcP primarily uses Asc in its plasma membrane localization and Cc in the mitochondria (Table 1).

The cysteine-protease cruzipain is an example of enzyme subcellular relocalization along the *T. cruzi* life cycle, where restriction to vesicles of the endosomal/lysosomal system in the epimastigote stage is relocalized to the parasite surface in the intracellular amastigote stage (45). The C-terminal extension in cruzipain was suggested to participate in this relocalization (46). *Tc*APx-CcP contains a positively charged 17-aa sequence of unknown function close to the carboxyl terminus (15) that could be involved in such enzyme relocalization.

To evaluate the significance of *Tc*APx-CcP in infectivity, studies using cultured cells and animals were performed. Two cellular models (macrophages and cardiomyocytes) were used for the in vitro infection studies. First, *T. cruzi* infection of naive macrophages leads to activation of the plasma membrane NADPH oxidase, yielding large amounts of superoxide radical, and subsequently H_2O_2 (due to superoxide dismutase-catalyzed dismutation), toward the internalized parasite (7, 47). Second, *T. cruzi* cardiomyocyte infection leads to the establishment of host–mitochondrial dysfunction with increased H_2O_2 production (39) that can diffuse and reach the intracellular amastigote. In

both cellular models, parasites overexpressing *Tc*APx-CcP were more infective than controls, thus supporting the hypothesis that this peroxidase plays a role in protecting *T. cruzi* from the cytotoxic effects of host cell-derived H_2O_2 (Fig. 9*A*). Recent proteomic data indicate that virulent *T. cruzi* strains express high levels of *Tc*APx-CcP, with this expression being further elevated in the infective stage (16, 48). However, it has now been shown that although *Tc*APx-CcP–null parasites are more susceptible to oxidant killing in vitro, the peroxidase activity is not a determinant for establishment of an infection in the animal model of CD, and is thus not essential for parasite survival within the mammalian host (20). As an ancient parasite, *T. cruzi* is well adapted to infect and persist in the mammalian host, developing redundant activities that have allowed it to succeed in hostile oxidative environments. Trypanosomes null for *Tc*APx-CcP contain other oxidant-metabolizing systems, including CPX, that are able to detoxify H_2O_2 efficiently and make parasite infection possible. For comparative purposes, the reaction rate values of H_2O_2 with *Tc*APx-CcP are 2.9×10^7 $M^{-1}{\cdot}s^{-1}$ (this work) and 3×10^7 $M^{-1}{\cdot}s^{-1}$ for CPX (49), supporting that both systems are, in principle, readily capable of eliminating cytotoxic levels of host cell-derived H_2O_2. Moreover, two other putative heme peroxidases are present in the parasite genome (TcCLB.507011.130 and TcCLB.511143.30), and the relevance of their expression under different biological conditions remains to be defined. Finally, and to assay the infectivity of *Tc*APx-CcP-overexpressing parasites, infection trials in two different mice lineages (BALB/c and C57BL/6) were conducted. Higher and significantly different parasitemias were observed in both mouse models of acute CD for the *Tc*APx-CcP overexpressers with respect to wt parasites, confirming its role in parasite virulence (Fig. 9*B*).

Overall, the data presented herein provide conclusive biochemical evidence of the hybrid nature of the type A heme peroxidase in *T. cruzi* (*Tc*APx-CcP); unravel mechanistic aspects of its redox enzymology with an atomic level of detail; and contribute to define its biological function, particularly its role as a virulence factor in CD.

Materials and Methods

Expression, Purification, and Site-Directed Mutagenesis of Recombinant *Tc*APx-CcP. The plasmid for heterologous expression of *Tc*APx-CcP (pTrcHis-APX) was kindly provided by Shane Wilkinson, Queen Mary University, London (15). Purification of recombinant enzymes was performed as done previously with minor modifications, as noted in *SI Materials and Methods* (15). Purity of *Tc*APx-CcP preparations was evaluated by 15% SDS/PAGE (Fig. S1), and the Soret peak at 409 nm for wt enzyme was used to quantitate the heme protein content (ε = 101 $mM^{-1}{\cdot}cm^{-1}$) (18). Site-directed mutagenesis of *Tc*APx-CcP (W233F) was performed using a site-directed mutagenesis kit with the following primers: forward, 5′-GGGCTACGTGGGTCCGTTCACG-CACGACAAG-3′, and reverse, 5′-CTTGTCGTGCGTGAACGGACCCACG-TAGCCC-3′. Sequence fidelity was confirmed by DNA sequencing (Institut Pasteur, Montevideo, Uruguay). The *Tc*APx-CcP W233F mutant was purified as described above for the wt enzyme, and the Soret peak at 414 nm was used to quantitate the heme protein content as described above. Protein concentration was measured by the Bradford protein assay.

Thiol Alkylation. Alkylation of wt and W233F *Tc*APx-CcP was carried out incubation of the enzyme (60 μM) with NEM (10 mM) for 2 h in phosphate buffer (100 mM, pH 7.4) at 4 °C. Excess NEM was immediately removed using HiTrap desalting columns (Amersham Biosciences) in PBS (100 mM, pH 7.4). Thiol alkylation was confirmed by the 5,5′-dithiobis-2-nitrobenzoic acid assay (50).

Spectroscopic Analysis. UV-visible spectra were recorded at 25 °C from Asc-free wt and W233F enzymes (2 μM) in the presence or absence of an equimolar H_2O_2 concentration in PBS (100 mM, pH 7.4).

Stopped-Flow Analysis. Rapid acquisition spectra and absorbance time courses were obtained following Asc-free wt and W233F enzymes before and after H_2O_2 addition by mixing equal amounts (4 μM each) in sodium phosphate buffer (100 mM, pH 7.4) containing diethylenetriaminepentaacetic acid (DTPA) (0.1 mM) at 10 °C, reaching a final concentration of 2 μM reagents. Absorbance was recorded with an Applied Photophysics SX-20 stopped-flow spectrofluorometer (mixing time of ≤2 ms) equipped with a rapid-scanning diode array. Formation of compound I species was followed at a Soret peak of 409 nm for wt and 414 nm for W233F enzyme.

Steady-State Activity Assays and Rate Constant Determinations. The steady-state activity assays for wt *Tc*APx-CcP and W233F mutant were performed using Asc and Cc^{2+} as reducing substrates, as previously described for *Lm*P (25, 26). The Cc was prereduced with dithionite, and the excess reductant was removed immediately using HiTrap desalting columns in phosphate buffer (100 mM, pH 7.4). The concentration of Cc^{2+} was calculated spectrophotometrically following absorbance at 550 nm ($\varepsilon_{550\ nm}$ = 8,900 and 29,900 $M^{-1}{\cdot}cm^{-1}$ for reduced and oxidized Cc, respectively). Assays were performed on a Cary UV-visible spectrophotometer at room temperature in sodium phosphate buffer (100 mM, pH 7.4). Both Asc- and Cc^{2+}-dependent peroxidase activities were assayed for the comparative analysis of wt *Tc*APx-CcP and W233F mutant. The oxidation of Asc was monitored at 290 nm (ε_{290} = 2,800 $M^{-1}{\cdot}cm^{-1}$) using *Tc*APx-CcP and W233F (0–1 μM) in the presence of H_2O_2 (40 μM) and Asc (200 μM). The Cc^{2+} oxidation was measured at 550 nm (ε_{550} = 21,000 $M^{-1}{\cdot}cm^{-1}$) using *Tc*APx-CcP (0.05–0.3 μM) and W233F (0.1–1 μM) in the presence of H_2O_2 (0–40 μM) and Cc^{2+} (50 μM). For the inactivation studies, wt *Tc*APx-CcP (2 μM) was mixed at 25 °C with H_2O_2 (8 μM), and aliquots were taken at different times (0–40 min). The activity was assayed as above using *Tc*APx-CcP (0.1 μM), Cc^{2+} (50 μM), and H_2O_2 (20 μM). For the bisubstrate kinetics analysis of the Cc^{2+}-dependent peroxidase activity of *Tc*APx-CcP, the assay was performed with increasing concentrations of H_2O_2 (0–50 μM) at four different concentrations of Cc^{2+} (4, 10, 25, and 60 μM). From a double reciprocal plot ($1/V_0$ versus $1/[Cc^{2+}]$), the apparent maximum velocity (V'_{max}) was determined at each concentration of Cc^{2+}. From the secondary plot $1/V'_{max}$ versus $1/[Cc^{2+}]$, real values for V_{max} and K_m (Cc^{2+}), respectively, were determined. The k (s^{-1}) value was obtained from the V_{max} value of substrate oxidation and considering the entire enzyme as the oxoheme complex intermediate, $k_{cat} = V_{max}/[E]$. A similar experimental approach was used for the determination of kinetic parameters for Asc (*SI Materials and Methods* and Fig. S2). For determination of the rate constant of the H_2O_2-dependent oxidation of *Tc*APx-CcP, the enzyme (2 μM) was rapidly mixed (using a stopped-flow spectrofluorometer) with H_2O_2 (0–12 μM), and the change in absorbance at 390 nm due to enzyme oxidation was recorded. Data were fitted to biexponential curves. The observed rate constant values (k_{obs}) for the fast and slow processes were plotted as a function of H_2O_2 concentration, and the second-order rate constants were determined from the slope of the plots.

EPR-Spin Trapping and Immunospin Trapping Studies of wt and W233F *Tc*APx-CcP. EPR spectra of Asc-free *Tc*APx-CcP, W233F mutant, and NEM-treated enzymes were recorded at room temperature (25 °C) on a MiniScope MS400 (Magnetech Instruments). For EPR experiments, the reaction mixture contained: wt or W233F (60 μM), DBNBS (10 mM) or DMPO (100 mM), H_2O_2 (60 μM), and DTPA (0.1 mM) in phosphate buffer (100 mM, pH 7.4). Immediately after oxidant addition, samples were transferred to a 100-μL flat cell and the spectra recorded within 1 min (one-spectrum acquisition). Instrumental conditions were as follows: microwave power, 20 mW; modulation amplitude, 2.5 G; time constant, 0.2 s; and scan rate, 1.67 G/s. For immunospin trapping, wt, W233F (10 μM), and NEM-treated enzymes were exposed to H_2O_2 (0–30 μM) in the presence of DMPO (100 mM). After treatment, proteins were subjected to SDS/PAGE, transferred to nitrocellulose membranes, and blocked in PBS (50 mM, pH 7.4) containing dry milk (5% wt/vol) for 1 h. Protein-DMPO adducts were detected using a chicken-derived polyclonal anti–DMPO-nitrone primary antibody (kindly provided by Ronald Mason, National Institutes of Environmental Health Sciences, Research Triangle Park, NC) and rabbit polyclonal anti-*Tc*APx-CcP (1:2,000 dilution in PBS) containing Tween-20 (0.1% vol/vol) and BSA (4% vol/vol) as previously described (5). Membranes were washed and then probed for 1 h with anti-chicken IgG (IR Dye-800; Licor Bioscience) and anti-rabbit IgG (IR Dye-680; Licor Bioscience) in PBS containing Tween 20 (0.1% vol/vol). Immunoreactive proteins were visualized with an infrared fluorescence detection system (Odyssey; Licor Bioscience).

MD Simulations. MD simulations for wt and W233F mutant *Tc*APx-CcP were performed. Both initial structures were generated by homology modeling using the Swiss-Model package (51), using the structure of *Lm*P solved at 1.76 Å resolution as a template, complexed with a heme prosthetic group and two cations: calcium and potassium (PDB ID code 3RIV). Both cations were kept in the systems, and the heme group was considered in the oxoferryl state. A pK_a prediction of ionizable protein residues was made with PROPKA (52). Considering the PROPKA-computed values and examining the structures, protonation states were assigned for ionizable residues, promoting hydrogen

bond formation. Because thiol/thiolate equilibrium may result critical in ET processes involving Cys residues, we also performed independent MD simulations for both protonation states of Cys^{222}. The systems were placed into a truncated octahedral box of three point transferable intermolecular potential (TIP3P) water model and optimized with two steps of energy minimization, each consisting of 400 cycles with a force constant of 500 kcal·mol^{-1}·Å^{-2} applied over all atoms, excluding water molecules in the former and over backbone atoms only in the latter. Temperature was increased from 0 to 10 K with 10-ps constant-volume MD, a time step of 0.1 fs, and a harmonic restraint potential of 50 kcal·mol^{-1}·Å^{-2} applied over all protein residues, ions, and ferryl-oxoheme. Thereafter, the temperature was raised from 10 to 300 K in 90-ps constant-volume MD with a 0.5-fs time step, applying a force constant of 10 kcal·mol^{-1}·Å^{-2} to the protein backbone atoms, ions, and ferryl-oxoheme. After heating, density was equilibrated with 400-ps MD simulation at a constant temperature and pressure with a time step of 1 ps and applying a force constant of 1 kcal kcal·mol^{-1}·Å^{-2} to the protein backbone atoms, ions, and ferryl-oxoheme. A Langevin thermostat was used for temperature control, whereas a Berendsen barostat was chosen to adjust the pressure to 1 bar (both regulated every 1 ps). Then, 100-ns-long MD simulations within the NTP ensemble were carried out, with a time step of 2 fs. All of the simulations were performed under periodic boundary conditions (53) using the SHAKE algorithm (54) to keep hydrogen atoms at equilibria bond lengths, and long-range electrostatics interactions were handled with Ewald sums, setting a cutoff distance of 10 Å. Parameters used for ferryl-oxoheme were taken from a study by Capece et al. (55).

ET Pathway Calculations. The probability of ET toward the ferryl-oxoheme group was calculated using the pathways algorithm (56, 57). This method looks for the best possible path connecting the electron donor and the acceptor, and it was successfully used by our group previously (58–62). Briefly, according to the Marcus theory (63), the ET rate constant (k_{ET}) depends on the reaction standard free energy ($\Delta G°$), the reorganization energy (λ), and the electronic coupling matrix (T_{DA}), described in the following equation:

$$k_{ET} = \frac{2\pi}{\hbar} |T_{DA}|^2 \frac{e^{-\frac{(\Delta G° + \lambda)^2}{4\lambda k_B T}}}{\sqrt{4\pi\lambda k_B T}},$$

where $\hbar$ is the Planck constant, k_B is the Boltzmann constant, and T is the system temperature. The pathways method estimates the T_{DA} for a given donor–acceptor couple, which is related to the probability of ET transfer, and thus directly involved in the resulting ET rate. Further details about parameters adjustments are provided by Ferreiro et al. (61). To compute the T_{DA} for each case, 400 representative snapshots from the last 80 ns of MD trajectories were used. All molecular visualization and drawings were performed with the Visual Molecular Dynamics program (64).

Peptide Mapping-MS Analysis of DMPO-Adducts After Reaction with H_2O_2. Mutant W233F (16 μM) enzymes were treated with equimolar concentrations of H_2O_2 in potassium phosphate buffer (100 mM, pH 7.4) at 25 °C in the presence of DMPO (100 mM). Excessive DMPO was removed by buffer exchange with ammonium bicarbonate buffer (50 mM, pH 8) using HiTrap desalting columns and enzyme-digested (overnight at 37 °C) with trypsin (trypsin/protein ratio of 20:1, sequencing grade; Promega). Tryptic digests were analyzed using a hybrid triple-quadruple linear ion trap mass spectrometer (QTRAP 4500; ABSciex) coupled online with a liquid chromatography system (Infinity 1260; Agilent). For the liquid chromatography-MS approach, peptides were separated on a reversed-phase column (Vydac 218TP; C18, 150 × 2.1 mm, 5 μm) and eluted with a linear gradient of acetonitrile (0.1% formic acid) from 0–45% in 90 min at a flow rate of 0.25 mL·min^{-1}. The electrospray voltage and declustering potential were set to 5.5 kV and 50 V, respectively, and the source temperature was 500 °C. Initial scanning was performed in the Q1 positive ion mode with the unit resolution at 1,000 Da·s^{-1} using a mass range of 300–2,000 Da·s^{-1}. Sequences from peptides of interest were performed by HPLC-tandem MS. Enhanced product ion analysis from selected peptide ions was performed using Q3 as a linear ion trap, with an optimized collision energy of 50 V and a mass range of 50–1,500 Da at 10,000 Da·s^{-1}. Data were acquired using Analyst 1.6.2 software (ABSciex) and analyzed using the BioTool Kit designed for PeakView 2.1 (ABSciex).

Parasites. *T. cruzi* epimastigotes (CL-Brener, wt) were cultured at 28 °C in brain heart infusion (BHI) containing heat-inactivated bovine fetal serum (10% vol/vol) as described previously (65). *T. cruzi* epimastigotes overexpressing *Tc*APx-CcP were obtained as described previously (5, 15). Transformed *Tc*APx-CcP (CL-Brener-pTEX-APX-9E10) overexpressing epimastigotes were cultured in BHI medium as above containing G418 (250 μg/mL; Sigma).

Immuno-EM Studies. The specificity of the antibodies used for the immunolocalization studies was evaluated by Western blot of protein extracts (10 μg) from rat-derived cardiomyocytes (H9c2; American Type Culture Collection) and from the different parasite stages (amastigotes, trypomastigotes, and epimastigotes; Fig. S5). Cardiomyocytes were seeded in culture flasks (25 cm^2) and infected as above. After 48 h of infection, an equal volume of a freshly prepared mixture of 4% paraformaldehyde (PFA; % vol/vol) and 0.4% glutaraldehyde (GA; % vol/vol) in sodium phosphate buffer (0.1 M, pH 7.4) was added to the cultures to reach a final concentration of 2% PFA and 0.2% GA (% vol/vol). The cells were fixed for 30 min at room temperature, after which the fixative was refreshed and kept at 4 °C. Samples were rinsed in sodium phosphate buffer (0.1 M, pH 7.4), and after overnight infiltration in sucrose (2.3 M), the cells were frozen in liquid nitrogen. Ultrathin cryosectioning and immunogold labeling were performed as described previously (66). Sections were picked up with a drop of a 1:1 mixture of sucrose (2.3 M) and 1.8% (vol/vol) methyl-cellulose (25 centipoise; Fluka AG), thawed, and transferred to formvar carbon-coated copper grids. The sections were subsequently immunolabeled at room temperature by floating on drops containing the diluted antibody [anti–*Tc*APx-CcP, anti-MPX, and antimonoclonal c-Myc9E10 antibody (Santa Cruz Biotechnology) and 10 nm of protein A gold]. After incubation, the sections were washed in distilled water, stained for 5 min with uranyl-oxalate (pH 7.0), washed again, and embedded in a mixture of 1.8% (vol/vol) methyl cellulose and 0.3% uranyl acetate at 4 °C. The sections were evaluated using a JEOL 1200CX electron microscope.

Cellular Infections. Parasites were differentiated to the infective metacyclic stage, and metacyclic forms were purified by overnight incubation with fresh human serum as previously described (5). Metacyclic trypomastigotes were used to infect confluent Vero cells (American Type Culture Collection) at 37 °C in a 5% CO_2 atmosphere. Culture-derived trypomastigotes were used to infect macrophages (J774A.1, ATCC-TIB-67; American Type Culture Collection) and cardiomyocytes (H9c2) cultured in DMEM (Sigma) supplemented with L-glutamine (2 mM), penicillin (100 units/mL), streptomycin (100 mg/mL), and heat-inactivated FBS (10% vol/vol) at 37 °C in a 5% CO_2 atmosphere. Macrophages and/or cardiomyocytes were seeded in Lab-Tek chamber slides and infected with culture-derived trypomastigotes from wt and *Tc*APx-CcP overexpressers (parasite/cell ratio of 5:1) (7). Nonengulfed parasites were removed by washing twice in Dulbecco's PBS at pH 7.4 (Sigma), and cells were further incubated for 24–96 h in DMEM at 37 °C. Infected cells were fixed in a 4% (vol/vol) fresh PFA solution in PBS for 10 min at room temperature, washed with PBS containing glycine (100 mM), and permeabilized for 5 min with 0.1% (vol/vol) Triton X-100 in PBS. The number of parasites per 100 macrophages and/or cardiomyocytes was determined by DAPI staining (5 μg/mL). Preparations were analyzed using a microscope (Nikon Eclipse TE-200) at a magnification of 1,000×, and digital photographs of infected cells were recorded. At least 2,500 cells from three independent experiments were counted. Results are expressed as the number of amastigotes per 100 cells and represent the mean of three independent experiments.

Animal Infections. Male BALB/c or female C57BL/6 mice (7–10 wk old, respectively) were inoculated i.p. (five mice per group) with culture-derived trypomastigotes (1.5×10^7 trypomastigotes) from wt (CL-Brener strain) or *Tc*APx-CcP overexpressers. The different susceptibility of these murine models to acute *T. cruzi* infection was previously characterized (67). Blood trypomastigote count (parasitemia) was assayed on blood (3 μL) drawn from the tail tips of mice, and the number of trypomastigotes per 32 fields was recorded from fresh blood in Neubauer chambers under a microscope (400× magnification).

Infection studies were approved by the Animal Ethics Committee (registration no. 070153-000119-5), registered with the Ethics Commission for the Use of Animals for Experimentation [Comisión de Ética en Uso de Animales (CEUA), Veterinary School, Uruguay], and mice were handled according to their guidelines.

ACKNOWLEDGMENTS. We thank Drs. Mike Davies and María Noel Alvarez for helpful comments and Drs. Adrián Aicardo, Mónica Marín, and Luciana Andrade for experimental advice. M.H., A.M., and M.M. were recipients of fellowships from the Agencia Nacional de Investigación e Innovación. This work was supported by grants (to R.R.) from the NIH (1R01AI095173) and Universidad de la República (Comisión Sectorial de Investigación Científica, Uruguay), from Biriden and Ridaline (to L.P. and R.R.) through the Fundación Manuel Pérez (Uruguay), and from Redoxoma Research, Innovation and Dissemination Center (to E.L. and O.A; Fundação de Amparo à Pesquisa do Estado de São Paulo Grant 2013/07937-8). Support was also obtained from the Progama de Desarrollo de Ciencias Básicas and Centro de Biología Estructural del Mercosur.

1. Bonney KM (2014) Chagas disease in the 21st century: A public health success or an emerging threat? *Parasite* 21:11.
2. Bern C, Kjos S, Yabsley MJ, Montgomery SP (2011) Trypanosoma cruzi and Chagas' Disease in the United States. *Clin Microbiol Rev* 24(4):655–681.
3. Luquetti AO, et al. (1986) Trypanosoma cruzi: Zymodemes associated with acute and chronic Chagas' disease in central Brazil. *Trans R Soc Trop Med Hyg* 80(3): 462–470.
4. Piacenza L, Peluffo G, Alvarez MN, Martínez A, Radi R (2013) Trypanosoma cruzi antioxidant enzymes as virulence factors in Chagas disease. *Antioxid Redox Signal* 19(7):723–734.
5. Piacenza L, et al. (2009) Enzymes of the antioxidant network as novel determiners of Trypanosoma cruzi virulence. *Int J Parasitol* 39(13):1455–1464.
6. Piacenza L, Alvarez MN, Peluffo G, Radi R (2009) Fighting the oxidative assault: The Trypanosoma cruzi journey to infection. *Curr Opin Microbiol* 12(4):415–421.
7. Alvarez MN, Peluffo G, Piacenza L, Radi R (2011) Intraphagosomal peroxynitrite as a macrophage-derived cytotoxin against internalized Trypanosoma cruzi: Consequences for oxidative killing and role of microbial peroxiredoxins in infectivity. *J Biol Chem* 286(8):6627–6640.
8. Carnieri EG, Moreno SN, Docampo R (1993) Trypanothione-dependent peroxide metabolism in Trypanosoma cruzi different stages. *Mol Biochem Parasitol* 61(1):79–86.
9. Boveris A, et al. (1980) Deficient metabolic utilization of hydrogen peroxide in Trypanosoma cruzi. *Biochem J* 188(3):643–648.
10. Comini MA, Flohé L (2013) Trypanothione-based redox metabolism of trypanosomatids. *Trypanosomatid Diseases: Molecular Routes to Drug Discovery*, eds Jäger T, Kock O, Flohé L (Wiley-VCH, Weinheim, Germany), pp 167–199.
11. Wilkinson SR, Temperton NJ, Mondragon A, Kelly JM (2000) Distinct mitochondrial and cytosolic enzymes mediate trypanothione-dependent peroxide metabolism in Trypanosoma cruzi. *J Biol Chem* 275(11):8220–8225.
12. Trujillo M, et al. (2004) Trypanosoma brucei and Trypanosoma cruzi tryparedoxin peroxidases catalytically detoxify peroxynitrite via oxidation of fast reacting thiols. *J Biol Chem* 279(33):34175–34182.
13. Piacenza L, et al. (2008) Peroxiredoxins play a major role in protecting Trypanosoma cruzi against macrophage- and endogenously-derived peroxynitrite. *Biochem J* 410(2):359–368.
14. Wilkinson SR, et al. (2002) TcGPXII, a glutathione-dependent Trypanosoma cruzi peroxidase with substrate specificity restricted to fatty acid and phospholipid hydroperoxides, is localized to the endoplasmic reticulum. *Biochem J* 364(Pt 3):787–794.
15. Wilkinson SR, Obado SO, Mauricio IL, Kelly JM (2002) Trypanosoma cruzi expresses a plant-like ascorbate-dependent hemoperoxidase localized to the endoplasmic reticulum. *Proc Natl Acad Sci USA* 99(21):13453–13458.
16. Atwood JA, 3rd, et al. (2005) The Trypanosoma cruzi proteome. *Science* 309(5733):473–476.
17. Clark D, Albrecht M, Arévalo J (1994) Ascorbate variations and dehydroascorbate reductase activity in Trypanosoma cruzi epimastigotes and trypomastigotes. *Mol Biochem Parasitol* 66(1):143–145.
18. Adak S, Datta AK (2005) Leishmania major encodes an unusual peroxidase that is a close homologue of plant ascorbate peroxidase: A novel role of the transmembrane domain. *Biochem J* 390(Pt 2):465–474.
19. Lad L, Mewies M, Raven EL (2002) Substrate binding and catalytic mechanism in ascorbate peroxidase: Evidence for two ascorbate binding sites. *Biochemistry* 41(46): 13774–13781.
20. Taylor MC, Lewis MD, Fortes Francisco A, Wilkinson SR, Kelly JM (2015) The Trypanosoma cruzi vitamin C dependent peroxidase confers protection against oxidative stress but is not a determinant of virulence. *PLoS Negl Trop Dis* 9(4):e0003707.
21. Zacks MA, Wen JJ, Vyatkina G, Bhatia V, Garg N (2005) An overview of chagasic cardiomyopathy: Pathogenic importance of oxidative stress. *An Acad Bras Cienc* 77(4):695–715.
22. Zámocký M, Furtmüller PG, Obinger C (2010) Evolution of structure and function of Class I peroxidases. *Arch Biochem Biophys* 500(1):45–57.
23. Zámocký M, Gasselhuber B, Furtmüller PG, Obinger C (2014) Turning points in the evolution of peroxidase-catalase superfamily: molecular phylogeny of hybrid heme peroxidases. *Cell Mol Life Sci* 71(23):4681–4696.
24. Logan FJ, Taylor MC, Wilkinson SR, Kaur H, Kelly JM (2007) The terminal step in vitamin C biosynthesis in Trypanosoma cruzi is mediated by a FMN-dependent galactonolactone oxidase. *Biochem J* 407(3):419–426.
25. Jasion VS, Polanco JA, Meharenna YT, Li H, Poulos TL (2011) Crystal structure of Leishmania major peroxidase and characterization of the compound i tryptophan radical. *J Biol Chem* 286(28):24608–24615.
26. Yadav RK, Dolai S, Pal S, Adak S (2008) Role of tryptophan-208 residue in cytochrome c oxidation by ascorbate peroxidase from Leishmania major-kinetic studies on Trp208Phe mutant and wild type enzyme. *Biochim Biophys Acta* 1784(5):863–871.
27. Pal S, Dolai S, Yadav RK, Adak S (2010) Ascorbate peroxidase from Leishmania major controls the virulence of infective stage of promastigotes by regulating oxidative stress. *PLoS One* 5(6):e11271.
28. Patterson WR, Poulos TL, Goodin DB (1995) Identification of a porphyrin pi cation radical in ascorbate peroxidase compound I. *Biochemistry* 34(13):4342–4345.
29. Erman JE, Vitello LB, Mauro JM, Kraut J (1989) Detection of an oxyferryl porphyrin pi-cation-radical intermediate in the reaction between hydrogen peroxide and a mutant yeast cytochrome c peroxidase. Evidence for tryptophan-191 involvement in the radical site of compound I. *Biochemistry* 28(20):7992–7995.
30. Thomson L, Trujillo M, Telleri R, Radi R (1995) Kinetics of cytochrome c2+ oxidation by peroxynitrite: Implications for superoxide measurements in nitric oxide-producing biological systems. *Arch Biochem Biophys* 319(2):491–497.
31. Trujillo M, et al. (2007) Pre-steady state kinetic characterization of human peroxiredoxin 5: Taking advantage of Trp84 fluorescence increase upon oxidation. *Arch Biochem Biophys* 467(1):95–106.
32. Dunford HB (1999) *Heme Peroxidases* (Wiley–VCH, New York).
33. Hiner AN, et al. (2000) Kinetic study of the inactivation of ascorbate peroxidase by hydrogen peroxide. *Biochem J* 348(Pt 2):321–328.
34. Yadav RS, Mishra P, Pandey AC (2008) Growth mechanism and optical property of ZnO nanoparticles synthesized by sonochemical method. *Ultrason Sonochem* 15(5): 863–868.
35. Detweiler CD, et al. (2002) Immunological identification of the heart myoglobin radical formed by hydrogen peroxide. *Free Radic Biol Med* 33(3):364–369.
36. Davies MJ, Gilbert BC, Haywood RM (1993) Radical-induced damage to bovine serum albumin: Role of the cysteine residue. *Free Radic Res Commun* 18(6):353–367.
37. Gatti RM, Radi R, Augusto O (1994) Peroxynitrite-mediated oxidation of albumin to the protein-thiyl free radical. *FEBS Lett* 348(3):287–290.
38. Slot JW, Geuze HJ (2007) Cryosectioning and immunolabeling. *Nat Protoc* 2(10): 2480–2491.
39. Gupta S, et al. (2009) Trypanosoma cruzi infection disturbs mitochondrial membrane potential and ROS production rate in cardiomyocytes. *Free Radic Biol Med* 47(10): 1414–1421.
40. Efimov I, et al. (2007) The redox properties of ascorbate peroxidase. *Biochemistry* 46(27):8017–8023.
41. Prütz WA, Butler J, Land EJ, Swallow AJ (1989) The role of sulphur peptide functions in free radical transfer: A pulse radiolysis study. *Int J Radiat Biol* 55(4):539–556.
42. Dolai S, Yadav RK, Pal S, Adak S (2009) Overexpression of mitochondrial Leishmania major ascorbate peroxidase enhances tolerance to oxidative stress-induced programmed cell death and protein damage. *Eukaryot Cell* 8(11):1721–1731.
43. Levine M, et al. (1996) Vitamin C pharmacokinetics in healthy volunteers: Evidence for a recommended dietary allowance. *Proc Natl Acad Sci USA* 93(8):3704–3709.
44. Radi R, Turrens JF, Freeman BA (1991) Cytochrome c-catalyzed membrane lipid peroxidation by hydrogen peroxide. *Arch Biochem Biophys* 288(1):118–125.
45. Tomás AM, Kelly JM (1996) Stage-regulated expression of cruzipain, the major cysteine protease of Trypanosoma cruzi is independent of the level of RNA1. *Mol Biochem Parasitol* 76(1-2):91–103.
46. Aslund L, et al. (1991) The C-terminal extension of the major cysteine proteinase (cruzipain) from Trypanosoma cruzi. *Mol Biochem Parasitol* 45(2):345–347.
47. Alvarez MN, Piacenza L, Irigoín F, Peluffo G, Radi R (2004) Macrophage-derived peroxynitrite diffusion and toxicity to Trypanosoma cruzi. *Arch Biochem Biophys* 432(2):222–232.
48. Zago MP, et al. (2016) TcI Isolates of Trypanosoma cruzi exploit the antioxidant network for enhanced intracellular survival in macrophages and virulence in mice. *Infect Immun* 84(6):1842–1856.
49. Piñeyro MD, Arcari T, Robello C, Radi R, Trujillo M (2011) Tryparedoxin peroxidases from Trypanosoma cruzi: High efficiency in the catalytic elimination of hydrogen peroxide and peroxynitrite. *Arch Biochem Biophys* 507(2):287–295.
50. Ellman GL (1959) Tissue sulfhydryl groups. *Arch Biochem Biophys* 82(1):70–77.
51. Biasini M, et al. (2014) SWISS-MODEL: Modelling protein tertiary and quaternary structure using evolutionary information. *Nucleic Acids Res* 42(Web Server issue): W252–W258.
52. Dolinsky TJ, et al. (2007) PDB2PQR: Expanding and upgrading automated preparation of biomolecular structures for molecular simulations. *Nucleic Acids Res* 35(Web Server issue):W522–W525.
53. Essman UPL, Berkowitz ML (1995) A smooth particle mesh Ewald method. *J Chem Phys* 103(19):8577–8593.
54. Ryckaert JPC, Ciccotti G, Berendsen HJC (1997) Numerical integration of the Cartesian equations of motion of a system with constraints: Molecular dynamics of n-alkanes. *J Comput Phys* 23:327–341.
55. Capece L, Lewis-Ballester A, Marti MA, Estrin DA, Yeh SR (2011) Molecular basis for the substrate stereoselectivity in tryptophan dioxygenase. *Biochemistry* 50(50):10910–10918.
56. Beratan DN, Betts JN, Onuchic JN (1991) Protein electron transfer rates set by the bridging secondary and tertiary structure. *Science* 252(5010):1285–1288.
57. Beratan DN, Onuchic JN, Winkler JR, Gray HB (1992) Electron-tunneling pathways in proteins. *Science* 258(5089):1740–1741.
58. Petruk AA, et al. (2012) Molecular basis of intramolecular electron transfer in proteins during radical-mediated oxidations: Computer simulation studies in model tyrosine-cysteine peptides in solution. *Arch Biochem Biophys* 525(1):82–91.
59. Alvarez-Paggi D, et al. (2010) Molecular basis of coupled protein and electron transfer dynamics of cytochrome c in biomimetic complexes. *J Am Chem Soc* 132(16):5769–5778.
60. Ly HK, et al. (2010) Thermal fluctuations determine the electron-transfer rates of cytochrome c in electrostatic and covalent complexes. *ChemPhysChem* 11(6):1225–1235.
61. Ferreiro DN, Boechi L, Estrin DA, Martí MA (2013) The key role of water in the dioxygenase function of Escherichia coli flavohemoglobin. *J Inorg Biochem* 119:75–84.
62. Martinez A, et al. (2014) Structural and molecular basis of the peroxynitrite-mediated nitration and inactivation of Trypanosoma cruzi iron-superoxide dismutases (Fe-SODs) A and B: Disparate susceptibilities due to the repair of Tyr35 radical by Cys83 in Fe-SODB through intramolecular electron transfer. *J Biol Chem* 289(18):12760–12778.
63. Marcus RJ (1956) Chemical conversion of solar energy. *Science* 123(3193):399–405.
64. Humphrey W, Dalke A, Schulten K (1996) VMD: Visual molecular dynamics. *J Mol Graph* 14(1):33–38.
65. Piacenza L, Peluffo G, Radi R (2001) L-arginine-dependent suppression of apoptosis in Trypanosoma cruzi: Contribution of the nitric oxide and polyamine pathways. *Proc Natl Acad Sci USA* 98(13):7301–7306.
66. Slot JW, Geuze HJ, Gigengack S, Lienhard GE, James DE (1991) Immuno-localization of the insulin regulatable glucose transporter in brown adipose tissue of the rat. *J Cell Biol* 113(1):123–135.
67. Bryan MA, Guyach SE, Norris KA (2010) Specific humoral immunity versus polyclonal B cell activation in Trypanosoma cruzi infection of susceptible and resistant mice. *PLoS Negl Trop Dis* 4(7):e733.

Supporting Information

Hugo et al. 10.1073/pnas.1618611114

SI Materials and Methods

Purification of Recombinant *Tc*APx-CcP wt and W233F Mutant Proteins. *Escherichia coli* BL21 DE3 cells containing the plasmid were grown at 37 °C in NZCYM broth containing ampicillin (50 μg/mL). Expression of recombinant *Tc*APx-CcP was induced by isopropyl-β-D-thiogalacto-pyranoside (0.8 mM) addition when the culture reached A_{600} = 0.6 in the presence of g-amino-levulinic acid (0.5 mM), and the temperature lowered to 22 °C for overnight protein expression. The purification was performed in a 5-mL HiTrap affinity column (Amersham Biosciences) charged with Ni^{2+} and equilibrated with binding buffer [50 mM sodium phosphate (pH 7.4), 10 mM imidazole, and 500 mM NaCl] at a flow rate of 3 mL·min^{-1}. *Tc*APx-CcP was eluted with a linear imidazole (10–500 mM) gradient in sodium phosphate [50 mM (pH 7.6) containing 500 mM NaCl]. Imidazole was removed immediately by buffer exchange in sodium phosphate buffer (50 mM, pH 7.4) using HiTrap desalting columns (Amersham Biosciences).

Controlled Digitonin-Mediated Cell Permeabilization and Western Blot Analysis. *Trypanosoma cruzi* epimastigotes overexpressing *Tc*APx-CcP (3×10^8 cells per milliliter, 1 mg of total parasite protein) were washed three times with 1 mL of Dulbecco's PBS (dPBS) at pH 7.4. The parasite pellet was resuspended in dPBS (1 mL) containing digitonin (0.1 mg/mL) and allowed to set for 5 min at 4 °C. Parasites were collected by centrifugation at 800 × *g* for 10 min, and the supernatant was recovered and kept on ice. The parasite pellet was washed three times (1 mL) with dPBS and resuspended in dPBS containing digitonin (0.1 mg/ mL). The procedure was repeated 10 times, reaching a final digitonin concentration of 1 mg. Proteins from the supernatants of each sequential extraction step, whole-parasite extract (total parasite extract), and the membrane-enriched fraction [remaining pellet after the last 0.1 mg/mL digitonin addition (total pellet extract)] were subjected to 15% SDS/PAGE, transferred to nitrocellulose membranes, and probed with anti-*T. brucei* Cc [kindly provided by Andre Schneider, University of Berne, Department of Chemistry and Biochemistry, Berne, Switzerland (63)], anti-*Tc*APx-CcP (1:2,000), anti-FeSOD-A, and anti-CPX (1:2,000).

Immunolocalization Studies. For fluorescence microscopy, wt epimastigotes (CL-Brener) were washed three times by centrifugation at 800 × *g* in PBS at pH 7.4 for 10 min and fixed in 4% (vol/vol) fresh PFA for 30 min at room temperature. Parasites were washed as above and permeabilized in PBS at pH 7.4 containing Triton X-100 (0.5% vol/vol) and BSA (3% wt/vol) for 30 min. Permeabilized parasites were incubated with rabbit anti-*Tc*APx-CcP and/or mouse anti–Fe-SODA polyclonal antibody (1:200) in the same solution and incubated overnight at 4 °C. Parasites were washed five times in PBS at pH 7.4 containing Triton X-100 (0.5% vol/vol) and incubated with anti-rabbit IgG-488 antibody and/or anti-mouse–PE (1/100; Invitrogen) for 1 h at room temperature. After staining, slides were mounted with antifade mounting solution plus DNA staining (DAPI) and visualized by epifluorescence microscopy (Eclipse TE-2000-E2-Nikon).

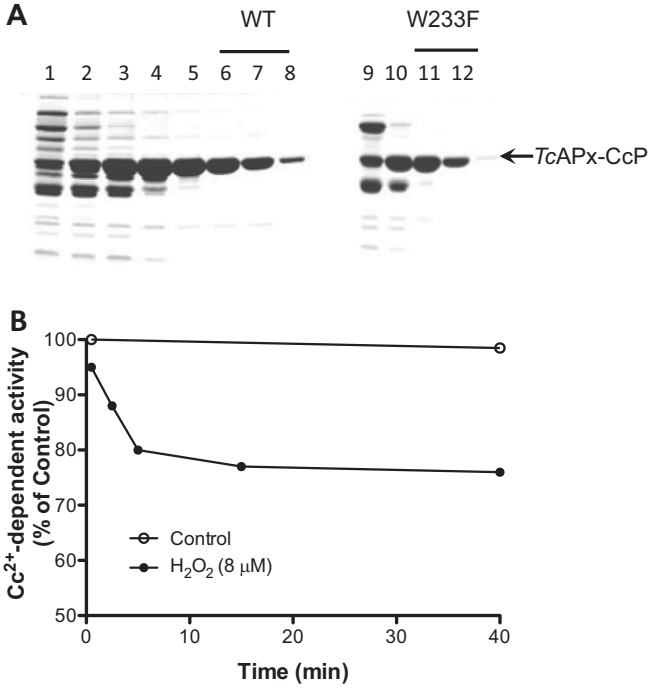

Fig. S1. (*A*) Purification of wt and W233F *Tc*APx-CcP. Protein fractions (lanes 1–8 and 9–12 for wt and W233F *Tc*APx-CcP mutant, respectively) obtained during purification of the His-tagged proteins using nickel-nitrilotriacetic acid affinity chromatography and eluted with a linear imidazole gradient were resolved on 15% SDS/PAGE and visualized by Coomassie blue staining. (*B*) Inactivation of *Tc*APx-CcP activity by H_2O_2. *Tc*APx-CcP (2 μM) was incubated with H_2O_2 (8 μM) in phosphate buffer (100 mM, pH 7.4) at 25 °C. At time intervals, aliquots of *Tc*APx-CcP (0.1 μM) were assayed for CcP activity (Cc^{2+}, 50 μM; H_2O_2, 10 μM) by following the decrease in absorbance at 550 nm due to oxidation of Cc^{2+} (ε value of 21,000 M^{-1}·cm^{-1}) in phosphate buffer. The data are expressed as a percentage of activity compared with the initial activity.

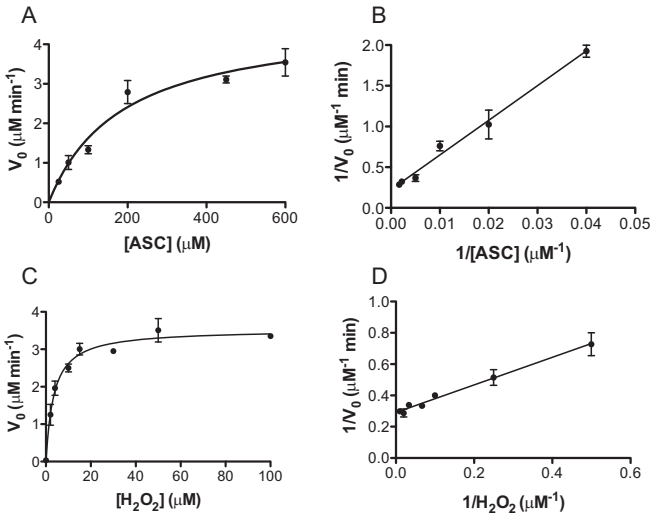

Fig. S2. Steady-state kinetic analysis of *Tc*APx-CcP with Asc. (*A*) Oxidation of Asc (0–600 μM) was monitored at 290 nm (ε_{290} = 2,800 $M^{-1}{\cdot}cm^{-1}$) using *Tc*APx-CcP (0.01 μM) in the presence of H_2O_2 (50 μM) in phosphate buffer (100 mM, pH 7.4). (*B*) From the double reciprocal plot (1/V_0 versus 1/[Asc]), a K_m value of 190 ± 2 μM for Asc was determined. (*C*) Asc-dependent peroxidase activity was assayed in the presence of Asc (600 μM) and different concentrations of H_2O_2 (0–100 μM) in phosphate buffer (100 mM, pH 7.4). (*D*) From the double reciprocal plot (1/V_0 versus 1/[H_2O_2]), a K_m value of 3 ± 0.5 μM for H_2O_2 was determined. The k_{cat} (s^{-1}) for the reaction of the reducing substrate was obtained from the V_{max} value of substrate oxidation of *B* and considering all of the enzyme as an oxoheme complex intermediate, $k_{cat} = V_{max}/[E]$. The k_{cat}/K_m for Asc was calculated at pH 7.4 (3.5×10^4 $M^{-1}{\cdot}s^{-1}$) being similar to the k_{cat}/K_m for Asc previously reported at pH 6.5 (Table 1).

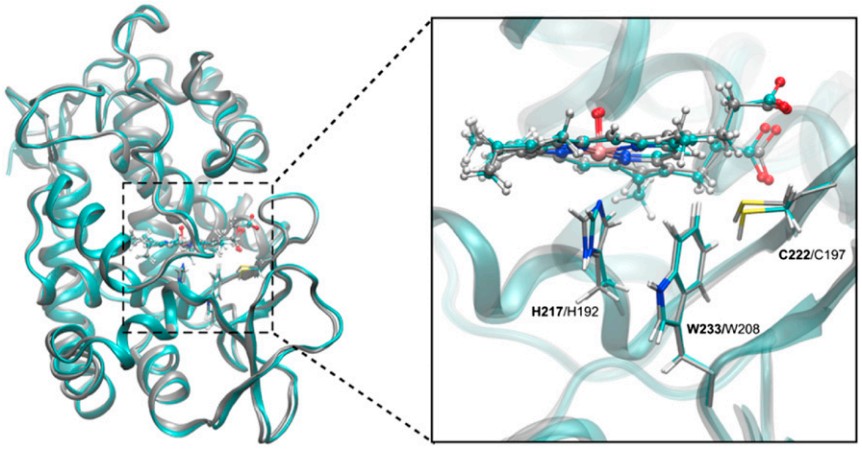

Fig. S3. (*Left*) Alignment of the *Lm*P crystallographic structure (cyan) with the *Tc*APx-CcP homology model (gray). Before superimposition, both systems were optimized, solvated, and equilibrated to 300 K, as described in *Materials and Methods*. (*Right*) Close-up image of the heme binding site. Side chains of His^{217}, Trp^{233}, and Cys^{222} (numbering in bold uppercase refers to *Tc*APx-CcP) are depicted by means of a "licorice" representation and colored by atom types, with the exception of carbon atoms, which are colored matched to the corresponding backbone (cyan for *Lm*P and gray for *Tc*APx-CcP).

A

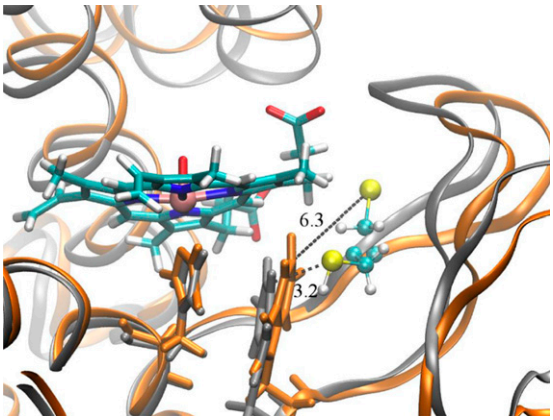

B

path	C222 protonation state	$<T_{DA}>$ (x10^{-2})	SD (x10^{-2})
W233→heme	R-SH	2.250	0.680
C222→heme	R-SH	4.780	2.861
C222→W233	R-SH	3.384	1.758
C222→heme (W233F)	R-SH	6.295	2.218
W233→heme	R-S$^-$	1.715	0.667
C222→heme	R-S$^-$	0.970	0.595
C222→W233	R-S$^-$	0.326	0.332
C222→heme (W233F)	R-S$^-$	0.043	0.020

Fig. S4. (*A*) Superimposition of representative structures of *Tc*APx-CcP with Cys^{222} in its two protonation states, obtained from MD simulations. The backbone of the structure, where Cys^{222} [as a thiolate (R-S^-)], colored in orange, and the corresponding thiol form (R-SH), colored in gray, is shown. Cys^{222} is depicted with a balls and sticks representation in both cases, and distances (in angstroms) between the S atom of Cys^{222} and the closer atom from Trp^{233} are shown as dashed lines. (*B*) ET coupling matrix average values ($<T_{DA}>$) and SDs in electron volts, obtained with the pathways algorithm.

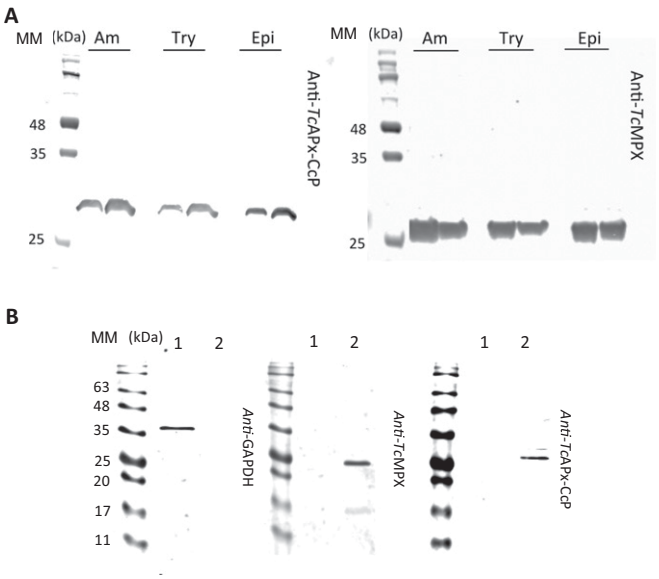

Fig. S5. Evaluation of the specificity of the *T. cruzi* antibodies used for immunolocalization studies. (*A*) Parasites extracts from *T. cruzi* amastigotes (Am), trypomastigotes (Try), and epimastigotes (Epi) (10 μg of total protein) run on 12% SDS/PAGE were probed with anti–*Tc*APx-CcP (*Left*, 1:2,000) or anti-*Tc*MPX (*Right*, 1:2,000) antibodies. For all parasites, stages analyzed in only one immunoreactive band were observed. (*B*) Western blot analysis to verify that there are no cross-reactive epitopes between *T. cruzi* antibodies and cardiomyocytes. Protein extracts from cardiomyocytes (lane 1, 100 μg) and *T. cruzi* epimastigotes (lane 2, 100 μg) were run on 15% SDS/PAGE and probed with anti-GAPDH (1:2,000; Sigma), anti-*Tc*MPX (1:2,000), and anti-*Tc*APx-CcP (1:2,000). *T. cruzi* antibodies did not cross-react with cardiomyocyte proteins. MM, molecular mass.

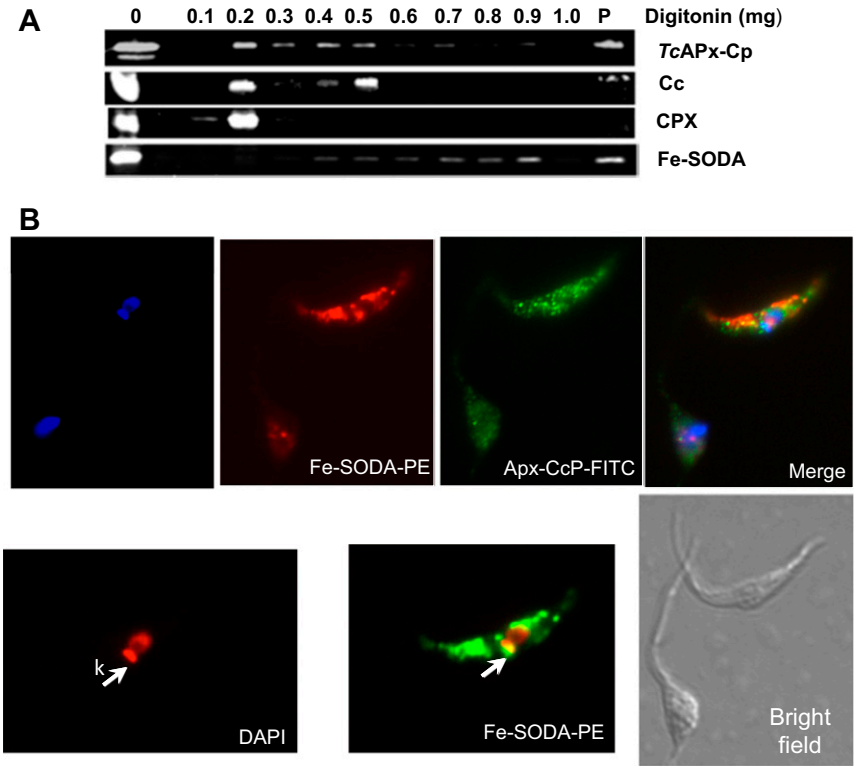

Fig. S6. (*A*) *T. cruzi* epimastigotes were permeabilized with sequential additions of digitonin (0.1 mg) by means of stepwise addition until reaching a final concentration of 1 mg of total digitonin (*SI Material and Methods*), and proteins released were analyzed by Western blot for the detection of *Tc*APx-CcP, mitochondrial Fe-SODA, anti-*T. brucei* Cc, and anti-CPX. P, pellet extract (membrane-enriched) fraction after the sequential addition of 0.1 mg of digitonin reaching a final concentration of 1 mg. Note that proteins immunodetected under each digitonin value represent a released fraction from the remaining protein left from the previous permeabilization steps. (*B*, *Upper*) Immunofluorescence microscopy of *T. cruzi* epimastigotes showing DNA staining (DAPI colored blue), Fe-SODA-PE (red), *Tc*APx-CcP (green-FITC), and a merged image. All panels correspond to the same image. (*B*, *Lower*) Colocalization (white arrows, merge colored yellow) of kinetoplastid (k) DNA (DAPI colored red) and Fe-SODA-PE (colored green). (*B*, *Lower Right*) Bright field of the image. All images were taken at 400× magnification.

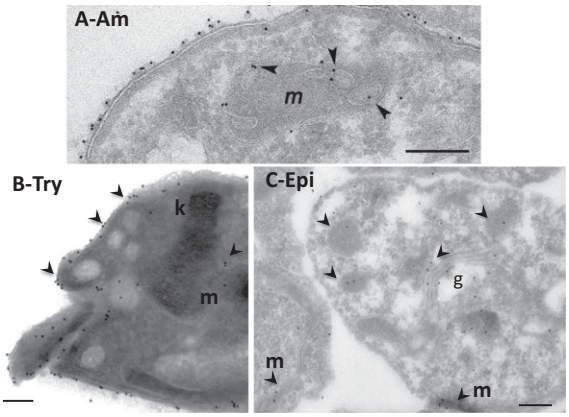

Fig. S7. *Tc*APx-CcP is confined to the plasma and mitochondrial membranes in the infective amastigote and trypomastigote stages. Immuno-EM localization of *Tc*APx-CcP in a culture-derived amastigote (*A*; Am), trypomastigote (*B*; Try), and axenic epimastigote (*C*; Epi) using a monoclonal antibody against the c-Myc9E10–tagged enzyme in *T. cruzi* overexpressers (CL-Brener-pTEX-APX-9E10). Labeling is abundant on the cell surface of amastigotes (*A*) and trypomastigotes (*B*) and is associated with limiting mitochondrial membrane and luminal membranes of the cristae (arrowheads) in all parasite stages. g, Golgi, k, kinetoplast; m, mitochondrion. (Scale bars: 200 nm.)

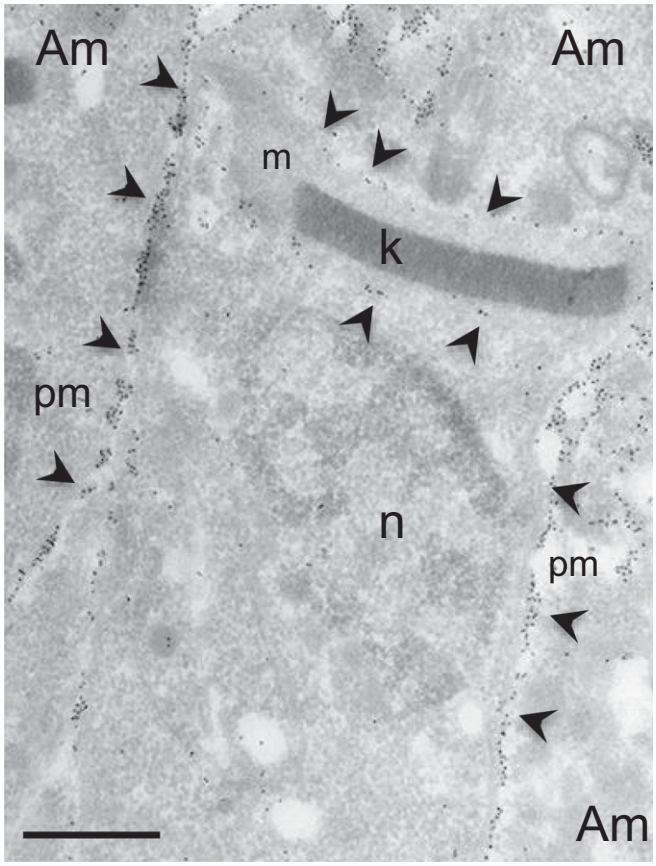

Fig. S8. *Tc*APx-CcP is localized to the plasma membrane and mitochondrion of intracellular *T. cruzi* amastigotes. Cultured cardiomyocytes infected with *T. cruzi* (wt) were analyzed with antisera raised against *Tc*APx-CcP by immuno-EM. The figure shows three intracellular amastigotes with abundant labeling at the plasma membrane (arrowheads) and associated with mitochondrial membranes (m, arrowheads). n, parasite nucleus; pm, plasma membrane. (Scale bar: 500 nm.)